

Universität Stuttgart

Master Thesis

**Automatic 3D lane marking
reconstruction using multi-view
aerial imagery**

Chun-Yu Sheu

Course of Study: GEOENGINE

Examiner: apl. Prof. Dr.-Ing. Norbert Haala

Supervisor: Dr.-Ing Franz Kurz

Commenced: 3. Juli 2017

Completed: 1. February 2018

Abstract

... This paper exploits the use of linear regression in image space for 3D line reconstruction.
[... will be finished after finishing all the chapters]

keywords: line reconstruction, linear regression, least-squares adjustment

Contents

1	Introduction	7
1.1	Motivation	7
1.2	3D Reconstruction	7
1.3	Digital Surface Model (DSM)	8
1.4	Issues in Line Matching	9
1.5	Related Work	9
1.6	Purpose	10
2	Methodologies	11
2.1	Lane markings Properties and Automatic Extraction	13
2.2	Imaging Properties of Aerial Photographs	15
2.3	Line Fitting	16
2.4	3D line reconstruction through nonlinear LS Adjustment	18
2.5	Line Projection on the DSM (Determination of Initial Parameter Estimates) .	24
3	Experimental Results and Evaluations	25
3.1	Materials	25
3.2	Preprocessing	32
3.3	Simulation	32
3.4	True Data	39
4	Conclusion and Future Work	43
A	LaTeX-Tipps	45
A.1	File-Encoding und Unterstützung von Umlauten	45
A.2	Zitate	45
A.3	Mathematische Formeln	46
A.4	Quellcode	46
A.5	Abbildungen	46
A.6	Tabellen	48
A.7	Pseudocode	48
A.8	Abkürzungen	50
A.9	Verweise	50
A.10	Definitionen	51
A.11	Fußnoten	51
A.12	Verschiedenes	51
A.13	Weitere Illustrationen	51
A.14	Plots with pgfplots	54

Contents

A.15 Figures with tikz	54
A.16 Schlusswort	55

1 Introduction

1.1 Motivation

The availability of large-scale, accurate high resolution 3D information of roads with lane markings and road furniture plays an important role towards autonomous driving. Such redundant sources of information for supporting the execution of dynamic driving task, such as localization, environmental perception and behavioral planning, is useful for increasing the robustness and availability of the system. Aerial imagery is a valuable database to derive 3D information of roads even in areas difficult to access, like on motorways. Compared to optical satellite data, acquiring large-scale 3D lane markings by optical aerial imagery is more efficient and has higher accuracy and spatial resolution. In view of the fact, that in Germany exists no area-wide 3D information of the road surface including lane markings, new methods to derive this information are demanded.

The standard workflow with aerial images would be to project the images onto a DSM and to derive the information in the projected imagery, but the generation of Digital Surface Model (DSM) from stereo images is challenging in the regions with low textures. The lane markings, for example, are the most visible texture on asphalt roads useful for 3D reconstruction. Thus, it is desired to improve the quality of the DSM on the road surfaces by exploiting the line character of the lane markings.

1.2 3D Reconstruction

Generally, the procedure of 3D objects reconstruction consists of feature extraction in image space and depth information recovery in object space. To reconstruct the depth information at the exposure moment, multi rays spatial intersection or single ray intersection with an elevation model can be applied. With Multi View Stereo (MVS) images and known Interior Orientation (IO) and Exterior Orientation (EO) of different images, spatial intersection is usually applied in the cases that the correspondences of the extracted features among different views can be established. Alternatively, when Digital Elevation Model (DEM) being available, single extracted feature can be directly projected onto the DEM. In this case, the quality of DEM directly influences the result of 3D reconstruction.

1.2.1 Feature Extraction and Matching

The aim of feature extraction is to gain the characteristics of the images, through which the stereo correspondence processes. As a result, the characteristics of the images closely link to the choice of matching methods. One of the appearance-based similarity measures for point (corner) features matching is NCC, which is the simplest but effective affine-illumination-invariant method.

Harris corner detector rotation-invariant

Scale-Invariant Feature Transform (SIFT) is proposed by Lowe in 1999 [D.G. Lowe 1999]. Lowe's approach transforms an image into a large collection of local feature vectors, also known as keypoint descriptors. Each SIFT feature descriptor is invariant to image translation, scaling, and rotation, partially invariant to illumination changes and affine or 3D projection. These SIFT keypoints are then matched by identifying their nearest neighbors.

sfm, sgm,

[However, it is challenging to apply line matching in practice. The reason is that extracted line features are often incomplete because of the defect of detectors or occlusions appearing in part of the lines. Moreover, the shapes, directions and surroundings of corresponding lane markings may be different in MVS, which makes line matching become failed (Schmid et al., 1997; Hofer et al., 2013).]. Line matching using space intersection to project lane markings to 3D object space

1.3 DSM

High resolution DSM can be generated by laser scanning or dense image matching. Compared to laser scanning, applying dense image matching to produce DSM is of lower cost and of shorter time for data collection. Dense image matching is to derive pixel-wise corresponding image points in MVS, and Semi-Global Matching (SGM), firstly proposed by Hirschmüller in 2008, is one of the most popular algorithm for dense image matching. SGM considers the information of entire image by means of aggregating matching cost along 8 or 16 cost paths, which not only enhances matching quality but also reduces computational complexity. However, lane markings are often located on homogeneous road surfaces, which makes the result of SGM become unstable. Therefore, 3D lane marking reconstructed by single aerial image and DSM is unstable and contains lots of noise.

Such high-resolution DSM gives a good starting point for the lane marking refinement. For semi-global matching, the matching step is cast into an energy minimization problem. The smoothness is not strong low texture area, not able to triangulate the 3D point, it took a min value as the height of that area -> systematic error

3D reconstruction using dense image matching is a hot topic as it enables the automatic extraction of 3D urban models, notably from airborne oblique imagery. However, applying DIM algorithms to oblique imagery is challenging because of large scale variations, illumination changes and the many occlusions.

1.4 Issues in Line Matching

Line matching is challenging for several reasons. First, line segments are often detected inexactly by automatic line detectors or occlusions appear in part of the lines. Thus the end-points of a line segment often do not correspond to each other in different views. Secondly, as mentioned above, there is no strong disambiguating geometric constraint available. Moreover, the corresponding neighborhoods may well have a very different shape and orientation, or even totally different surroundings when dealing with wiry objects. [C. Schmid et al 1997] [M. Hofer et al Feb. 2013]

1.5 Related Work

C. Schmid et al. [C. Schmid et al. 1997] exploit the epipolar geometry of line segments and the one-parameter family of homographies to provide point-wise correspondences, allowing cross-correlation of patches around line segments along the candidate lines in the epipolar-beam-region for matching scores evaluation.

Considering the facts that the neighborhood of line segments may be of poorly textured or the surrounding area of a line segment on the intersection of two planes may have very different affine shape changes in different long base-line views, line segments are barely comparable using classical correlation patches yet the color neighborhood along this line segment undergoes only slight changes. Based on color histogram rather than textures, H. Bay et al. [H. Bay et al. 2005] exploit the appearance similarity of line segment pairs and their topological layout to iteratively increase the correct matches. If region matches are available, they are automatically integrated in the topological configuration and exploited in combination. The final coplanar grouping stage allows to estimate the fundamental matrix even from line segments only. While color provides a very strong cue for discrimination, it may fail in the case where color feature is not distinctive, e.g. gray images. Besides, the advantage of matching groups of line segments is that more geometric information is available for disambiguation, the disadvantage is the increased computational complexity [C. Schmid et al. 1997].

Without resorting to any other constraints or prior knowledge, Z. Wang et al. [Z. Wang et al. May. 2009] propose a purely image content-based line descriptor MSLD for automatic line segments matching. Adapting SIFT-like strategy, MSLD is highly distinctive and robust against image rotation, illumination change, image blur, viewpoint change noise, JPEG compression and partial occlusion [Z. Wang et al. May. 2009]

1 Introduction

The above appearance-based approaches demand either constant and rich neighboring textures or similar color profile of line segments, they are technically matching the surroundings instead of the lines themselves.

1.1.3 3D line Reconstruction without Matching

In order to create 3D models without the need of explicit line matching, A. Jain et al. [A. Jain et al. 2010] generate all possible hypothetical straight 3D line segments by triangulating the detected straight 2D line segments from different views, then they keep the one whose back projection on the gradient images of neighboring views has the highest score, assuming that line segments correspond to high gradient areas in images. Built upon the same principles whilst applying epipolar constraint on line segment end-points, M. Hofer et al. generate less hypothetical 3D line segments and thus increase performance significantly while still creating accurate results. However, both approaches are barely possible in the case of infinite line reconstruction, where the detected 2D lines in different views do not exactly correspond to the same part of a 3D line.

Taylor et al. [C. J. Taylor et al. 1995] formulate the Structure from Motion (SfM) problem in terms of minimization of an objective function that measures the total squared distance in the image plane between the observed edge segments and the projections of the reconstructed lines. By reconstructing the infinite straight line that supports the observed edge segments rather than the end-points of the line, the algorithm can be used even when multiple edges in a single image correspond to different portions of the same 3D line.

1.6 Purpose

In this thesis, I develop a framework to automatically detect the lane markings in the unprojected aerial imagery, and to refine the 3D information of the road surface by exploiting the line character of the lane markings.

[solve the problem of (quasi)infinite and curved lane markings] [apply standard line detection algorithms for automatic lane marking detection] [use of aerial image data set with special flight configuration at both sides of the motorway]

The unprojected aerial images with their bundle-adjusted orientations and the DSM are the inputs of my research. By sliding a window of reasonable length and width through the curved long lane lines, the collected line segment in the current window is assumed to be straight. I investigate the use of linear regression to optimize the location of each line segments in object space so that its back projection would best fit the detected 2D line in all the covering views, i.e. the position and height of each 3D lane marking segments will be refined in one optimization step.

The framework will be tested on aerial imagery from the German highway A9 and validated with ground measured lane markings by GPS.

dem Buch [WSPA] zu tun. Satz eine neue Zeile im .tex-Dokument anzufangen.

2 Methodologies

The following sections introduce the principles of 3D lane marking reconstruction method of this work, with the work flow shown in Figure 2.1.

Section 2.1 describes the applied standard line detection algorithm for labeling the lane markings. To relate the object coordinates of a point with its image coordinates, Section 2.2 introduces the imaging properties of aerial images and their mathematical models, including the collinearity equation and lens distortion correction.

Section 2.3 presents the principle of line fitting and further derives the nonlinear Least-Squares (LS) model for line equations in two-point form. With the combination of the extended collinearity equation introduced in Section 2.2, Section 2.4 elaborates the usage of line fitting for 3D lane marking reconstruction.

In Section 2.5 the problem of acquiring initial values is described, as initial values of unknown quantities are required in nonlinear LS model. Section 2.7??? demonstrates how the corresponding measurements in image space are collected given the initial values in object space.

2 Methodologies

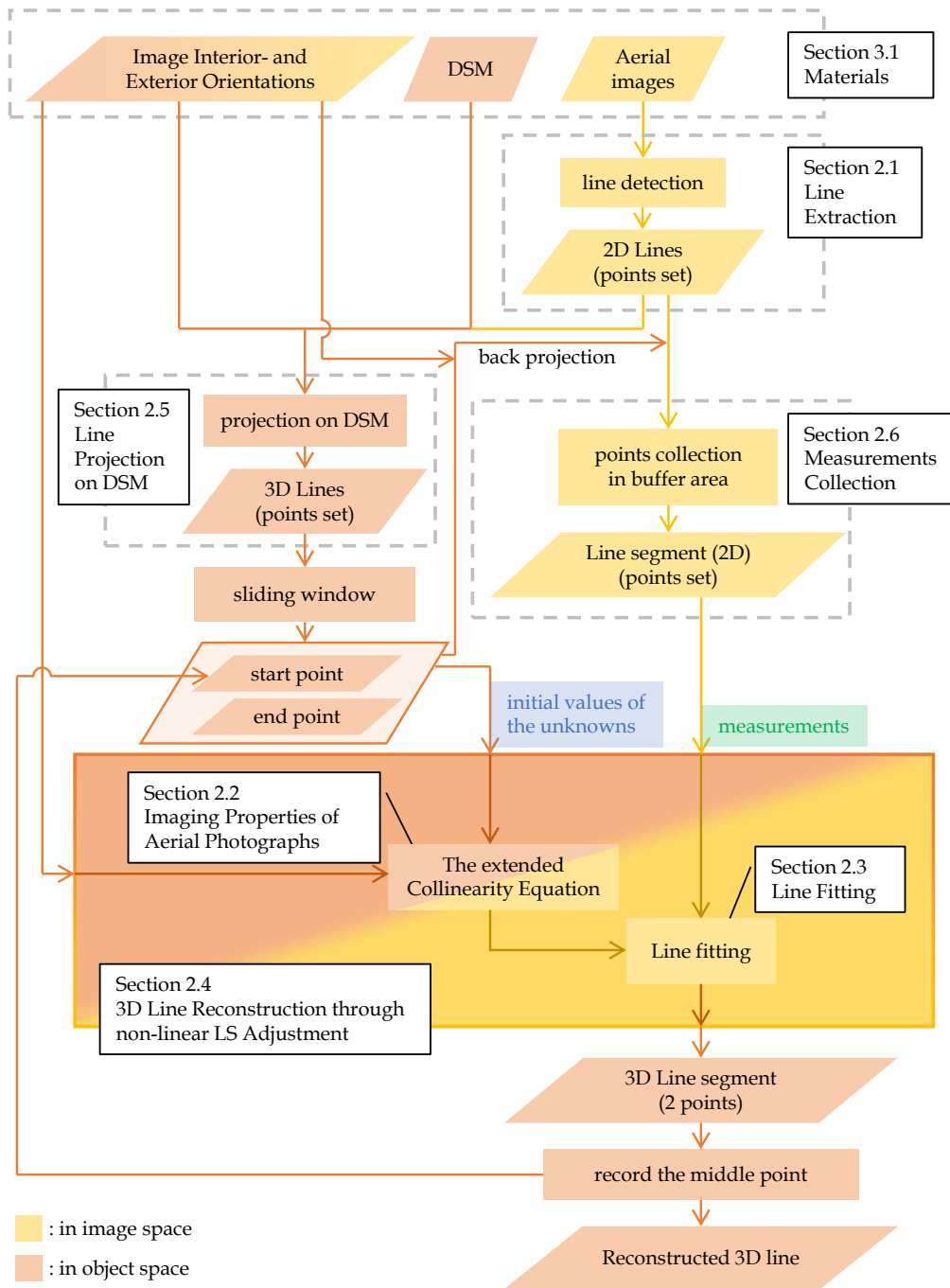


Figure 2.1: The work flow

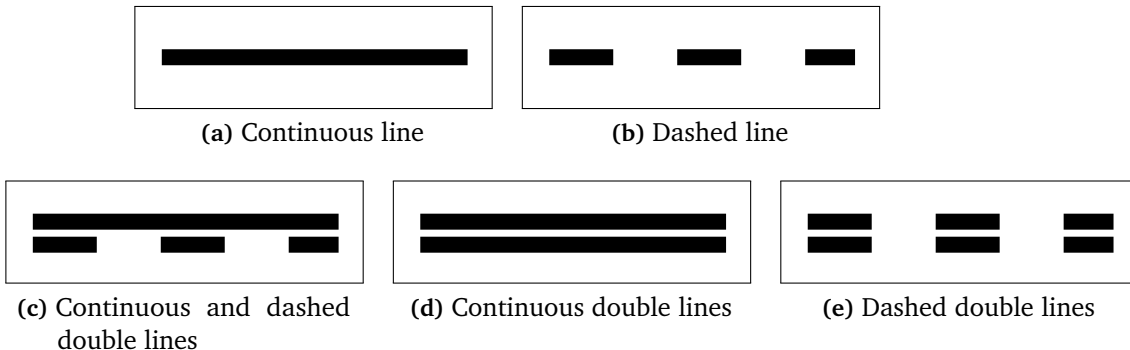


Figure 2.2: Line types of lane markings [source RMS Teil 1]

2.1 Lane markings Properties and Automatic Extraction

2.1.1 Line Detector

The appearance of lane markings on German roads including line type, color and width is specified depending on the road type. Different line types of lane markings are shown in Figure 2.2 and their line widths are defined in Table 2.1. As shown in Table 2.2, the dashed lane markings on motorways are of 6 meter length.

Because of the appearance, the problem of lane marking detection can be treated as a line detection problem. We restrict the proposed framework to lane markings with single white lines (dashed or continuous) of 0.3 meter width. Other types like in restricted zone, double lines, parking areas, temporal yellow lines in construction sites etc, are excluded.

There are many approaches for line detection operators. Prewitt line detector uses two orthogonal gradient operators, and the pixels in the operators are of same weights. Sobel detector also uses two orthogonal gradient operators, but the weights of pixel in operators are not equal. The closer the pixel to the center of operator, the higher weight it has. Canny detector searches local extrema of gradient to locate the positions of line features. Edge drawing (Topal & Akinlar, 2012) first spots anchors along rows and columns by Sobel detector, and then joins these anchors to extract line features.

In this work, the principle to extract line features is to firstly derive the line direction for each pixel by using partial derivatives of a Gaussian smoothing kernel. Pixels that have a local maximum in the second directional derivative perpendicular to the line direction are marked as line points. By thresholding their second directional derivative values, the accepted line points are then linked and connected. The resultant connected points which compose a line are of sub-pixel precision. Figure 2.3 shows the extracted lines on the masked original image.

¹and corresponding roads in the sense of the VwV-StVO to § 42 to mark 330 (motorway) II

2 Methodologies

	motorways ¹	other roads
narrow lines	0.15 [m]	0.12 [m]
wide lines	0.30 [m]	0.25 [m]

Table 2.1: Widths of lane markings [source RMS Teil 1]

	motorways	other roads	
		in town	out of town
line / gap	6 [m] / 12 [m]	3 [m] / 6 [m]	4 [m] / 8 [m]

Table 2.2: Lengths of dashed lane markings with ratio 1:2 [source RMS Teil 1]

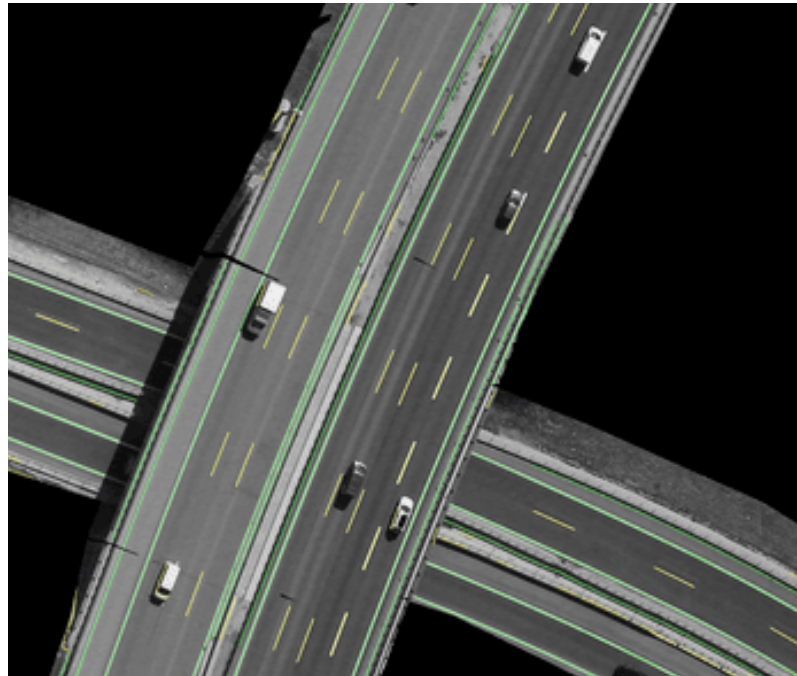


Figure 2.3: Lane markings Extraction. The extracted long lane-lines are marked in green and the dashed ones are in yellow. Note that both cases are reconstructed into 3D with the same framework; different colors here are only for illustration.

2.2 Imaging Properties of Aerial Photographs

This section describes the geometric model of the projection of 3D points into the image generated by a real camera. We first restrict the discussion in Section 2.2.1 to central perspective projection where the collinearity equation originate from. We then model deviations from this model, addressing real cameras with imperfect lenses, in Section 2.2.2.

2.2.1 Collinearity Equations

We assume frame photography, i.e. photographs exposed on a frame chip in one instant, and assume central projection model with cameras that have a single viewpoint and a planar sensor and being straight line-preserving. Collinearity indicates the condition that the image point (on the sensor plate of the camera), the observed point (in object space) and the projection center of the camera were aligned at the moment the picture was taken. Every measured point leads to two collinearity equations, describing transformations from object space to image coordinates:

$$\begin{aligned} x &= x_0 - c \frac{R_{11}(X - X_0) + R_{21}(Y - Y_0) + R_{31}(Z - Z_0)}{R_{13}(X - X_0) + R_{23}(Y - Y_0) + R_{33}(Z - Z_0)} \\ y &= y_0 - c \frac{R_{12}(X - X_0) + R_{22}(Y - Y_0) + R_{32}(Z - Z_0)}{R_{13}(X - X_0) + R_{23}(Y - Y_0) + R_{33}(Z - Z_0)} \end{aligned} \quad (2.1)$$

where

(x, y) : image coordinates of the point

(x_0, y_0) : image coordinates of principal point

c : principal distance; focal length

(X, Y, Z) : object coordinates of the point

(X_0, Y_0, Z_0) : object coordinates of projection center

R_{11}, \dots, R_{33} : elements of the rotation matrix R (orthogonal 3×3 -matrix from object space to image space, with 3 independent angles ω , ϕ and κ)

2.2.2 Lens Distortion Correction

An original image appears to have some degree of deviations from perspective mapping due to lens distortion, lens refraction or non-planarity of the sensor surface. There are several models to describe these perturbing effects and can be used to undistort the images, resulting in rectified images which are now straight line-preserving.

A subset of physical distortion model [Fraser 1997] is chosen, with two radial symmetric distortion parameters A_1 and A_2 , two asymmetric parameters B_1 and B_2 , and a scaling C_1 and an affine shearing parameter C_2 . Assuming x and y to be the distorted image coordinates, the corrections Δx and Δy are then calculated by the following equations:

$$\begin{aligned} \Delta x &= x_p + A_1 x_* (r^2 - R_0^2) + A_2 x_* (r^4 - R_0^4) + B_1 (r^2 + 2x_*^2) + B_2 2x_* y + C_2 y \\ \Delta y &= y_p + A_1 y (r^2 - R_0^2) + A_2 y (r^4 - R_0^4) + B_1 (r^2 + 2y^2) + B_2 2x_* y \end{aligned} \quad (2.2)$$

2 Methodologies

with $r = \sqrt{x_*^2 + y^2}$, $x_* = \frac{x}{C_1}$ and radius² R_0 being set to a third of the sensor diagonal.

The undistorted image coordinates x' and y' are then calculated by

$$\begin{aligned} x' &= x + \Delta x \\ y' &= y + \Delta y \end{aligned} \quad (2.3)$$

2.2.3 Extended Collinearity Equation

As real cameras generally only approximate the perspective camera model, lens distortion correction can be additionally included in the collinearity model, attempting to correct the pixel position so that they obey the perspective model with sufficient accuracy.[W. Förstner et al. 2016]

By inserting (2.1) and (2.2) into (2.3) , the relationship between a 3D point $\mathbf{P}(X, Y, Z)$ and its corresponding distorted image coordinates $\mathbf{p}(x, y)$ can be described as

$$\begin{aligned} x &= x_0 - c \frac{R_{11}(X - X_0) + R_{21}(Y - Y_0) + R_{31}(Z - Z_0)}{R_{13}(X - X_0) + R_{23}(Y - Y_0) + R_{33}(Z - Z_0)} \\ &\quad - (x_p + A_1 x_*(r^2 - R_0^2) + A_2 x_*(r^4 - R_0^4) + B_1(r^2 + 2x_*^2) + B_2 2x_* y + C_2 y) \\ y &= y_0 - c \frac{R_{12}(X - X_0) + R_{22}(Y - Y_0) + R_{32}(Z - Z_0)}{R_{13}(X - X_0) + R_{23}(Y - Y_0) + R_{33}(Z - Z_0)} \\ &\quad - (y_p + A_1 y(r^2 - R_0^2) + A_2 y(r^4 - R_0^4) + B_1(r^2 + 2y^2) + B_2 2x_* y) \end{aligned} \quad (2.4)$$

To express (2.4) shortly, a function \mathcal{G} is defined as

$$\mathbf{p} = \mathcal{G}(\mathbf{q}, \mathbf{P}) \quad (2.5)$$

which takes the interior and exterior orientations as well as the lens distortion parameters of a camera $\mathbf{q}(x_0, y_0, c, X_0, Y_0, Z_0, R_{11}, \dots, R_{33}, A_1, A_2, B_1, B_2, C_1, C_2)$ and the position of a 3D point $\mathbf{P}(X, Y, Z)$, and returns the corresponding distorted image coordinates $\mathbf{p}(x, y)$.

2.3 Line Fitting

Line fitting is the process of constructing a infinite straight line that has a best fit to a 2D dataset. One of the approaches is linear regression which attempts to find the linear function that "best" predicts the dependent variable values as a function of the independent variable. In this work, "best" predict will be understood as in the LS approach: minimization of the sum of squared residuals (differences between the measured and the estimated values of the dependent variable).

²At the radius R_0 the radial symmetric distortion is zero by definition, which avoids too high distortion values at the edges and reduces the correlation with the focal length.

In the case of standard linear regression, the regressor y is assumed error free, inconsistencies³ are only for the dependent variable x . Geometrically it means that the horizontal distances from observed data to the fitted line is minimized. To minimize the perpendicular distances from the data points to the regression line, a orthogonal regression model is derived in Section 2.3.1.

For a later combination with point-wise extended collinearity equation (2.5) in next section, we aim to fit the line equation in two-point form to the observed dataset. For such nonlinear least squares fitting purpose, a nonlinear mixed model is derived in Section 2.3.2.

A functional model is unsolvable when the assumed "dependent" variable is indeed not a function of the independent variables, i.e. the assumed functional relationship does not really exist. Take an observed set of 2D points with their Cartesian coordinates $\{x_i, y_i\}_{i=1}^n$ on a vertical line $x = \text{constant}$ for example. Their y values have no dependency on their x values, i.e. knowledge of x tells nothing about y . Therefore, for this dataset, the functional model $y = f(x)$ is barely solvable. In such cases, however, x is a function of y (which is actually a constant function) and the equation system which models the dependent variable x being a function of the independent variable y becomes solvable. Regarding the dataset used in this work (which will be described with more details in Section 3.1) where the observed 2D points scatter mainly in column direction in image space, the linear relationship between x and y values will be setup as $x = f(y)$ to avoid weakly solvable equations system.

2.3.1 Orthogonal Regression

A linear regression model describes a dependent variable as a linear function of the regressor (an independent variable). Given a dataset $\{x_i, y_i\}_{i=1}^n$ of n points on a 2D plane, in the case when both dependent variable x_i and regressor y_i are measured with errors , a linear regression model takes the form:

$$x_i - e_{x_i} = a_0 + a_1 \bar{y}_i \quad (2.6)$$

where the regression coefficients a_0 and a_1 are the unknown parameters to be estimated, \bar{y}_i denotes the true but unobserved regressor, and the error variable e_{x_i} is an unobserved random variable that adds noise to the linear relationship between the dependent variable x and true regressor \bar{y}_i . The true regressor \bar{y}_i is observed with an error e_{y_i} in the pseudo observation equation:

$$y_i - e_{y_i} = \bar{y}_i \quad (2.7)$$

Such models, as the combination of (2.6) and (2.7), that account the measurement errors in both dependent variable and regressor, are errors-in-variables models. Further more, for the case of equal error variances, i.e. when $\delta = \frac{\sigma_{e_x}}{\sigma_{e_y}} = 1$, it is a orthogonal regression model which minimizes the perpendicular distances from the data points to the regression line.

³The word "inconsistencies" indicates the unobserved random errors, also called as measurement errors.

2 Methodologies

2.3.2 Orthogonal Regression in Two-point Form

The two-point form of a infinite line in the Cartesian plane passing through the points (x_1, y_1) and (x_2, y_2) is given by:

$$(x - x_1) = \frac{(x_2 - x_1)}{(y_2 - y_1)} \times y - y_1 \quad (2.8)$$

with $y_2 \neq y_1$, where (x, y) is any point on the line.

Let the unknown coordinates of two different points on a line in 2D space be (x_1, y_1) and (x_2, y_2) and the observed 2D points be $\{x_i, y_i\}_{i=1}^n$ with measurement errors e_{x_i} and e_{y_i} in both variables. The orthogonal regression model in two-point form:

$$x_i - e_{x_i} = (x_1 - \frac{(x_2 - x_1)}{(y_2 - y_1)} \times y_1) + \frac{(x_2 - x_1)}{(y_2 - y_1)} \times \bar{y}_i \quad (2.9)$$

$$y_i - e_{y_i} = \bar{y}_i \quad (2.7 \text{ revisited})$$

To express (2.9) and (2.7) shortly, a function \mathcal{F} is defined as

$$\hat{\mathbf{p}} = \mathcal{F}(\mathbf{p}_s, \mathbf{p}_e, y) \quad (2.10)$$

which takes 2D coordinates of a start-point $\mathbf{p}_s(x_s, y_s)$ and an end-point $\mathbf{p}_e(x_e, y_e)$ that define an infinite line, and takes the measured y-coordinate y of an image point $\mathbf{p}(x, y)$, and returns the estimated image coordinates $\hat{\mathbf{p}}(\hat{x}, \hat{y})$ which lies on the infinite line $\overline{\mathbf{p}_s \mathbf{p}_e}$.

Note that as a combination of (2.9) and (2.7), function \mathcal{F} is actually composed of

$$\begin{aligned} \hat{x} &= \mathcal{F}^x(\mathbf{p}_s, \mathbf{p}_e, y) \\ \hat{y} &= \mathcal{F}^y(\mathbf{p}_s, \mathbf{p}_e, y) \end{aligned} \quad (2.11)$$

2.4 3D line reconstruction through nonlinear LS Adjustment

In this section, I describe the process of refining the position of a 3D line segment in the object space so that its back-projection in each image has a best-fit to the extracted line in the image space. To simplify the problem, a lane-marking-segment is partially reconstructed through a sliding window in the object space. Each segment is approximated by a straight line, taking into account the maximum curvature of the highway. The length of the sliding window depends on the expected curvature, and for motorways it was fixed to 9m ...

In the sliding window, a line segment is reconstructed taking into account all the measurements (the detected lines) collected in the corresponding regions in all covering images. Only the middle point of the sliding window is then reconstructed by the least-squares estimator (see chapter xx) and is recorded. The sliding window then moves half length forward, and the process of 3D reconstruction started again from the recorded middle

point of the previous line segment. Another line segment is then reconstructed, with its middle point being recorded. These recorded middle points are in the end the nodes of the reconstructed line. The reconsideration in overlapping region makes the reconstruction more robust.

In Section 2.4.1 I firstly set up a model of observation equations. They describe the fitting of a straight line to the measurements in each covering image, where the fitting lines on different images are transformed from a single 3D straight line segment through the extended collinearity equation (2.4).

Regarding the fact that the collinearity is a point-wise condition, a line segment is represented by its two endpoints whose object coordinates are the six unknown parameters in the LS model. Correspondingly, the observation equations are line equations in two-point form. A line equation has however a mathematical meaning of infinite length. Therefore, some constraints on unknowns are necessary to avoid arbitrary locations of the two points on the infinite reconstructed 3D line. The constraint equations are modeled in Section 2.4.1.

2.4.1 The Nonlinear Gauss-Markov Model with Constraints

Given are the N observations $\mathbf{l} = [l_n]$, $n = 1, 2, \dots, N$, from which the U unknown parameters $\mathbf{x} = [x_u]$, $u = 1, 2, \dots, U$ are to be determined, with generally $U \leq N$.

The nonlinear Gauss-Markov model with N nonlinear functions $\mathbf{f}(\mathbf{x}) = [f_n(\mathbf{x})]$, $n = 1, 2, \dots, N$ and the H nonlinear constraints $\mathbf{h}(\hat{\mathbf{x}}) = [h_\eta(\hat{\mathbf{x}})]$, $\eta = 1, 2, \dots, H$ ($H < U$) between the unknowns can be written as:

$$\mathbf{l} + \hat{\mathbf{v}} = \mathbf{f}(\hat{\mathbf{x}}) \quad \text{or} \quad \hat{\mathbf{l}} = \underset{N \times 1}{\mathbf{f}}(\hat{\mathbf{x}}) \quad (2.12)$$

$$\underset{H \times 1}{\mathbf{h}}(\hat{\mathbf{x}}) = \mathbf{0} \quad (2.13)$$

where the observations \mathbf{l} are explicit functions of the unknowns \mathbf{x} , with the additive residuals \mathbf{v} introduced to the observations \mathbf{l} to achieve consistency.

Assuming that the deviations between the observed values \mathbf{l} and the true values $\hat{\mathbf{l}}$ are of random nature and have normal (or Gaussian) distribution, the uncertain observations \mathbf{l} are modeled with first and second moments:

$$\mathbf{l} \sim \mathcal{N}(\mathbf{f}(\hat{\mathbf{x}}), \Sigma_{ll}) \quad (2.14)$$

where Σ_{ll} is the variance-covariance matrix of observations \mathbf{l} .

!!!! same statistical dispersion

$$\Sigma_{ll} = \mathbb{D}(\mathbf{l}) = \mathbb{D}(\mathbf{v}) = \mathbb{D}(\hat{\mathbf{l}}) \quad (2.15)$$

The task is to minimize the weighted sum of residuals:

$$\Omega = \frac{1}{2}(\mathbf{l} - \mathbf{f}(\mathbf{x}))^T(\mathbf{l} - \mathbf{f}(\mathbf{x})) \quad \text{such that} \quad \mathbf{h}(\mathbf{x}) = \mathbf{0} \quad (2.16)$$

with the assumption of equal-weighted observations.

2 Methodologies

The nonlinear equation system is approximated to be locally linear with small step size of the unknown quantities. The linearized form is expressed as:

$$\widehat{\Delta l} = \Delta l + \widehat{v} = \underset{N \times U}{A} \widehat{\Delta x} \quad (2.17)$$

$$c_h = \underset{H \times U}{H^T} \widehat{\Delta x} \quad (2.18)$$

where

the $N \times U$ design matrix, which is the Jacobian of the function evaluated at the approximate values of the unknown parameters, is

$$A = \left. \frac{\partial f(x)}{\partial x} \right|_{x=\widehat{x}^a}$$

the $U \times H$ constraint matrix, which is the Jacobian of the constraints, is

$$H = \left. \left(\frac{\partial h(x)}{\partial x} \right)^T \right|_{x=\widehat{x}^a}$$

and the residual constraints are

$$c_h = -h(\widehat{x}^a)$$

with the corrections

$$\Delta l = l - f(\widehat{x}^a) =: \widehat{v}^a \quad (2.19)$$

$$\widehat{\Delta x} = \widehat{x} - \widehat{x}^a \quad (2.20)$$

where \widehat{x}^a is the approximate values for the estimates of the unknown parameters.

In the linearized substitute model as shown in (2.17) and (2.18), it turns to solve for the increments of unknowns Δx instead of the unknowns themselves. The LS estimation is applied iteratively until convergence is achieved.

The unknown parameters $\widehat{\Delta x}$ of the linearized model can be determined from the extended normal equation system

$$\begin{bmatrix} A^T A & H \\ H^T & 0 \end{bmatrix} \begin{bmatrix} \widehat{\Delta x} \\ \lambda \end{bmatrix} = \begin{bmatrix} A^T \Delta l \\ c_h \end{bmatrix} \quad (2.21)$$

The matrix A does not need to have full rank, but the block matrix $[A_T, H]$ must have full rank in order to guarantee the estimation problem has a unique solution.

The redundancy R of the problem is

$$R = N + H - U \quad (2.22)$$

Observation Equations

Given a start-point $\mathbf{P}_s(X_s, Y_s, Z_s)$ and an end-point $\mathbf{P}_e(X_e, Y_e, Z_e)$ of a line segment L in the object space and the camera parameters \mathbf{q}^j of camera j . Consider the case where there are J images covering this line segment. With the expanded collinearity model (2.4), the start- and end-points of this line segment's back-projection in image j have the image coordinates $\mathbf{p}_s^j(x_s^j, y_s^j)$ and $\mathbf{p}_e^j(x_e^j, y_e^j)$:

$$\begin{aligned}\mathbf{p}_s^j &= \mathcal{G}(\mathbf{q}^j, \mathbf{P}_s) \\ \mathbf{p}_e^j &= \mathcal{G}(\mathbf{q}^j, \mathbf{P}_e)\end{aligned}\quad \forall j = 1, 2, \dots, J \quad (2.23)$$

Let l^j be the corresponding line segment of L being extracted (observed) on image j . Given a dataset $\{x_{l,i}^j, y_{l,i}^j\}_{i=1}^{N_l^j}$ of N_l^j points on line segment l^j , their estimated image coordinates $\hat{\mathbf{p}}_{l,i}^j(\hat{x}_{l,i}^j, \hat{y}_{l,i}^j)$ on the infinite line $\overline{\mathbf{p}_s^j, \mathbf{p}_e^j}$ computed from the orthogonal regression model (2.27) are:

$$\hat{\mathbf{p}}_{l,i}^j = \mathcal{F}(\mathbf{p}_s^j, \mathbf{p}_e^j, y_{l,i}^j) \quad \forall i = 1, 2, \dots, N_l^j \quad (2.24)$$

Combining (2.23) with (2.24) gives function \mathcal{H} :

$$\begin{aligned}\hat{\mathbf{p}}_{l,i}^j &= \mathcal{F}(\mathcal{G}(\mathbf{q}^j, \mathbf{P}_s), \mathcal{G}(\mathbf{q}^j, \mathbf{P}_e), y_{l,i}^j) \\ &= \mathcal{H}(\mathbf{q}^j, \mathbf{P}_s, \mathbf{P}_e, y_{l,i}^j) \quad \forall i = 1, 2, \dots, N_l^j, \quad \forall j = 1, 2, \dots, J\end{aligned} \quad (2.25)$$

which takes camera parameters $\mathbf{q}^j(x_0, y_0, c, X_0, Y_0, Z_0, R_{11}, \dots, R_{33}, A_1, A_2, B_1, B_2, C_1, C_2)$, object coordinates of \mathbf{P}_s and \mathbf{P}_e which define a line $\overline{\mathbf{P}_s, \mathbf{P}_e}$, and the observed y-coordinate of the point $\mathbf{p}_{l,i}^j$ in image space, and returns the estimated image coordinates $\hat{\mathbf{p}}_{l,i}^j$ on the back projected line of $\overline{\mathbf{P}_s, \mathbf{P}_e}$.

Corresponding to Equation (2.11), function \mathcal{H} is composed of

$$\begin{aligned}\hat{x}_{l,i}^j &= \mathcal{H}^x(\mathbf{q}^j, \mathbf{P}_s, \mathbf{P}_e, y_{l,i}^j) \\ \hat{y}_{l,i}^j &= \mathcal{H}^y(\mathbf{q}^j, \mathbf{P}_s, \mathbf{P}_e, y_{l,i}^j)\end{aligned}\quad \forall i = 1, 2, \dots, N_l^j, \quad \forall j = 1, 2, \dots, J \quad (2.26)$$

Equation (2.26)

Since the adjustment will be done "segment-wise"— for a pair of P_s and P_e , the measurements will be collected correspondingly. Thus the subscription l representing specific line segment will be left out in the followings.

2 Methodologies

Each image gives $2 \times N^j$ observation equations⁴. These equations are often stacked together and written in vector form as:

$$\begin{bmatrix} x_1^j \\ x_2^j \\ \vdots \\ x_{N^j}^j \\ y_1^j \\ y_2^j \\ \vdots \\ y_{N^j}^j \end{bmatrix} \stackrel{\cdot}{=} \begin{bmatrix} \mathcal{H}^x(\mathbf{q}^j, \hat{\mathbf{P}}_s, \hat{\mathbf{P}}_e, y_1^j) \\ \mathcal{H}^x(\mathbf{q}^j, \hat{\mathbf{P}}_s, \hat{\mathbf{P}}_e, y_2^j) \\ \vdots \\ \mathcal{H}^x(\mathbf{q}^j, \hat{\mathbf{P}}_s, \hat{\mathbf{P}}_e, y_{N^j}^j) \\ \mathcal{H}^y(\mathbf{q}^j, \hat{\mathbf{P}}_s, \hat{\mathbf{P}}_e, y_1^j) \\ \mathcal{H}^y(\mathbf{q}^j, \hat{\mathbf{P}}_s, \hat{\mathbf{P}}_e, y_2^j) \\ \vdots \\ \mathcal{H}^y(\mathbf{q}^j, \hat{\mathbf{P}}_s, \hat{\mathbf{P}}_e, y_{N^j}^j) \end{bmatrix} \left\{ \begin{array}{l} N^j \\ N^j \end{array} \right\} \quad (2.27)$$

For all covering image $j = 1, 2, \dots, J$, there are $2 \times \sum_{j=1}^J N^j$ observation equations. Being written in the structure of the Gauss-Markov model, corresponding to Equation (2.12), they are expressed as:

$$l + \hat{v} = f(\hat{x}) : \begin{bmatrix} x_1^1 \\ \vdots \\ x_{N^1}^1 \\ y_1^1 \\ \vdots \\ y_{N^1}^1 \\ \vdots \\ y_{N^J}^J \\ \vdots \\ x_{N^J}^J \\ \vdots \\ x_{N^J}^J \\ y_1^J \\ \vdots \\ y_{N^J}^J \end{bmatrix} + \begin{bmatrix} \hat{v}_{x_1^1} \\ \vdots \\ \hat{v}_{x_{N^1}^1} \\ \hat{v}_{y_1^1} \\ \vdots \\ \hat{v}_{y_{N^1}^1} \\ \vdots \\ \hat{v}_{y_{N^J}^J} \\ \vdots \\ \hat{v}_{x_{N^J}^J} \\ \vdots \\ \hat{v}_{x_{N^J}^J} \\ \hat{v}_{y_1^J} \\ \vdots \\ \hat{v}_{y_{N^J}^J} \end{bmatrix} = \begin{bmatrix} \mathcal{H}^x(\mathbf{q}^1, \hat{\mathbf{P}}_s, \hat{\mathbf{P}}_e, y_1^1) \\ \vdots \\ \mathcal{H}^x(\mathbf{q}^1, \hat{\mathbf{P}}_s, \hat{\mathbf{P}}_e, y_{N^1}^1) \\ \mathcal{H}^y(\mathbf{q}^1, \hat{\mathbf{P}}_s, \hat{\mathbf{P}}_e, y_1^1) \\ \vdots \\ \mathcal{H}^y(\mathbf{q}^1, \hat{\mathbf{P}}_s, \hat{\mathbf{P}}_e, y_{N^1}^1) \\ \vdots \\ \vdots \\ \vdots \\ \mathcal{H}^x(\mathbf{q}^J, \hat{\mathbf{P}}_s, \hat{\mathbf{P}}_e, y_1^J) \\ \vdots \\ \mathcal{H}^x(\mathbf{q}^J, \hat{\mathbf{P}}_s, \hat{\mathbf{P}}_e, y_{N^J}^J) \\ \mathcal{H}^y(\mathbf{q}^J, \hat{\mathbf{P}}_s, \hat{\mathbf{P}}_e, y_1^J) \\ \vdots \\ \mathcal{H}^y(\mathbf{q}^J, \hat{\mathbf{P}}_s, \hat{\mathbf{P}}_e, y_{N^J}^J) \end{bmatrix} \left\{ \begin{array}{l} 2 \times N^1 \\ \vdots \\ 2 \times N^J \end{array} \right\} \quad (2.28)$$

⁴Dot equal indicates inconsistencies between the measured values, x_i^j and \hat{x}_i^j , and the computed values, $\mathcal{H}^x(q^j, P_s, P_e, y_i^j)$ and $\mathcal{H}^y(q^j, P_s, P_e, y_i^j)$.

Constraint Equations

There are three constraints on the unknown parameters used in this work:

- Fixing the X-, Y-coordinates of the start-point using the approximate values:

$$\hat{X}_s - X_s^0 = 0 \quad (2.29)$$

$$\hat{Y}_s - Y_s^0 = 0 \quad (2.30)$$

- Fixing the length of the line segment (i.e. constraining the relative location of the end-point):

$$\sqrt{(\hat{X}_s - \hat{X}_e)^2 + (\hat{Y}_s - \hat{Y}_e)^2 + (\hat{Z}_s - \hat{Z}_e)^2} - S = 0 \quad (2.31)$$

Only in the first line segment reconstruction of a long lane marking, the fixed X_s and Y_s values are from the initial parameter estimates derived in Section 2.5. Starting from the second line segment, the fixed values X_s^0 and Y_s^0 depend on the previously determined values.

The constraint equations (2.29), (2.30) and (2.31) can be stacked together and written in the structure of the Gauss-Markov model with constraints, corresponding to Equation (2.13):

$$h(\hat{x}) = \mathbf{0} : \begin{bmatrix} \hat{X}_s - X_s^0 \\ \hat{Y}_s - Y_s^0 \\ \sqrt{(\hat{X}_s - \hat{X}_e)^2 + (\hat{Y}_s - \hat{Y}_e)^2 + (\hat{Z}_s - \hat{Z}_e)^2} - S \end{bmatrix} = \begin{bmatrix} 0 \\ 0 \\ 0 \end{bmatrix} \quad (2.32)$$

Least-Squares Estimation of the non-linear Gauss-Markov Model with Constraints

Since the estimated variance-covariance matrix of the estimated parameters $\hat{\Sigma}_{\hat{X}\hat{X}}$ depends on both the design matrix A (i.e. the configuration) and the posterior standard deviation $\hat{\sigma}_0$ (i.e. the posterior measurements quality):

$$\hat{\Sigma}_{\hat{X}\hat{X}} = \hat{\sigma}_0^2 (A^T A)^{-1} = \begin{bmatrix} \hat{\sigma}_{\hat{X}}^2 & \hat{\sigma}_{\hat{X}\hat{Y}} & \hat{\sigma}_{\hat{X}\hat{Z}} \\ \hat{\sigma}_{\hat{Y}\hat{X}} & \hat{\sigma}_{\hat{Y}}^2 & \hat{\sigma}_{\hat{Y}\hat{Z}} \\ \hat{\sigma}_{\hat{Z}\hat{X}} & \hat{\sigma}_{\hat{Z}\hat{Y}} & \hat{\sigma}_{\hat{Z}}^2 \end{bmatrix} \quad (2.33)$$

we are not able to tell from the variances $\hat{\sigma}_{\hat{X}}$, $\hat{\sigma}_{\hat{Y}}$, $\hat{\sigma}_{\hat{Z}}$ whether the .

By setting a constant priori standard deviation value in all the LS adjustment processes (i.e. assuming the measurements are of same quality in each segment), the priori variance-covariance matrix of the estimated parameters $\Sigma_{\hat{X}\hat{X}}$ reflects the quality of the design matrix (i.e. the configuration strength) in each LS adjustment processes.

$$\Sigma_{\hat{X}\hat{X}} = \sigma_0^2 (A^T A)^{-1} \quad (2.34)$$

2.5 Line Projection on the DSM (Determination of Initial Parameter Estimates)

As the equation system in Section 2.4 may exhibit multiple local minimum, a "correct" initial approximation of the unknowns is required for convergence to the correct solution. To provide such initial 3D line segment, the extracted line features derived in Section 2.1 can be projected onto DSM based on the bundle adjusted exterior and interior orientations.

Given image coordinates $\mathbf{p}(x, y)$ of a point and (bundle-adjusted) image orientations \mathbf{q} , there is still one degree of freedom in extended collinearity equation (2.5) on solving object coordinates $\mathbf{P}(X, Y, Z)$. Combined with the usage of DSM, which provides the height information Z given a position (X, Y) , the corresponding object coordinates can be solved iteratively until the increment ΔZ small enough, i.e. convergence achieved.

Considering that the DSM is raster (discrete) whereas X and Y have continuous numerical values, the DSM height is bilinear interpolated during the iterative process.

3 Experimental Results and Evaluations

Section 3.1 provides information about input dataset and the applied preprocessing steps.

In Section 3.3, the correctness of the derived LS model for reconstruction is evaluated. Some other properties of the proposed reconstruction approach are also discussed.

3.1 Materials

Aerial Images For real-time mapping applications during disasters, mass events and traffic monitoring scenarios, the German Aerospace Center (DLR) has developed a new optical sensor system— the 4k system— on a helicopter from DLR. The oblique aerial images used in this work are acquired from a Canon EOS 1D-X camera, one of the three non-metric cameras in the 4k system, with an oblique viewing angle τ of 15° . The image data sets used in this work were acquired in around 500m flying height $H_{fliheight}$ above ground, which leads to a GSD of 7cm.

An example aerial image is shown in Figure 3.5. Table 3.1 lists the properties of this camera, and Table 3.2 provides the viewing geometry information.

The images used in this work are acquired with a special flight configuration at both sides of the motorway which guarantees a continuous stereo view perpendicular to the lane marking direction.¹ This is realized by flying at the right-hand side with respect to flying direction along the motorway, with the left oblique camera looking left-down to the motorway, in both forward and backward trip. The flight configuration is shown in Figure 3.1 on the Google Earth platform.

Besides, the forward overlap is around 70%, and all the lane markings are covered by both strips, whereas the side overlap depends on the distance of flight strips, which are a result of the pilots navigation ability and other influences, like wind. Nevertheless, the motorway in its entire width was covered by the two flight strips. Altogether, this results in approximately 8-image coverage in road areas.

¹The classical photogrammetric approach on flight planning is to have several straight flight lines which cover the whole motorway in a stereo view. This would be possible in this project yet would require more flight costs and would produce many more images.

3 Experimental Results and Evaluations

Canon EOS 1D-X	
Lenses	Zeiss Makro Planar 2/50
Sensor / Pixel size	Full frame CMOS / $6.944 \mu\text{m}$
Image size	5184×3456 pixel, ratio 3:2 (17.9 MPix)
ISO	100–204800
max. frame rate / max. images	14 fps/ 180 images
Exposure time	30 s – 1/8000 s
Data interface	LAN (EDSDK software interface)

Table 3.1: Properties of the oblique camera

RGB, 50mm lens	
Viewing directions	$\pm 15^\circ$
FOV	$\pm 34^\circ$ across strip, $\pm 13^\circ$ along strip
Coverage @500m	780 m \times 230 m
GSD @500m	6.9 cm (nadir)

Table 3.2: Viewing geometry



Figure 3.1: Flight trajectory of DLR helicopter visualized on the Google Earth platform. The green polyline shows the flight trajectory. *Source: Google Earth 04/01/2017*

Exterior and Interior Orientations The EO of the images are directly measured by a GNSS/Inertial system IGI II. The EO parameters are then refined by a self-calibrating bundle adjustment. The accuracies of the exterior orientation (EO) parameters are shown in Table 3.3. The calibrated IO parameters and their accuracies are shown in Table 3.4. To provide an overall quality on the interior orientations: from the calibration result of interior orientations (involving lens distortion), the residuals appear non-systematic and the biggest residual $r_{max,IO}$ is around 1 pixel.

To judge the influence of exterior and interior parameters on positioning accuracy in object space, the maximum values for each component based on the flight configuration was calculated. The quality of interior and exterior orientation parameters set would have a maximum impact in object space for around 16.5 [cm] in X,Y-direction:

- caused by inaccurate camera position:

$$\sqrt{\sigma_{north}^2 + \sigma_{east}^2} = \sqrt{0.055^2 + 0.035^2} \approx 0.065 \text{ [meter]}$$

- caused by inaccurate camera attitude:

$$\begin{aligned} & \tan(\sqrt{\sigma_{roll}^2 + \sigma_{pitch}^2}) \times H_{flightheight} \times \frac{1}{\cos^2 \tau} \\ &= \tan(\sqrt{0.002^2 + 0.002^2}) \times 500 \times \frac{1}{\cos^2 15^\circ} \approx 0.026 \text{ [meter]} \end{aligned}$$

- caused by inaccurate Interior Orientations:

$$r_{max,IO} \times GSD \times \frac{1}{\cos^2 \tau} = 1 \times 0.069 \times \frac{1}{\cos^2 15^\circ} \approx 0.074 \text{ [meter]}$$

and around 9.4 [cm] in Z-direction:

- caused by inaccurate camera position:

$$\sigma_{altitude} \approx 0.069 \text{ [meter]}$$

- caused by inaccurate camera attitude:

$$\begin{aligned} & \tan(\sqrt{\sigma_{roll}^2 + \sigma_{pitch}^2}) \times H_{flightheight} \times \frac{\sin \tau}{\cos \tau} \\ &= \tan(\sqrt{0.002^2 + 0.002^2}) \times 500 \times \frac{\sin 15^\circ}{\cos 15^\circ} \approx 0.007 \text{ [meter]} \end{aligned}$$

- caused by inaccurate Interior Orientations:

$$r_{max,IO} \times GSD \times \frac{\sin \tau}{\cos \tau} = 1 \times 0.069 \times \frac{\sin 15^\circ}{\cos 15^\circ} \approx 0.018 \text{ [meter]}$$

The above information tells the positioning accuracy in object space with measurements on a single image. With corresponding measurements from multiple stereo views, which allows the intersection of multiple rays, the positioning accuracy is expected to be improved for being overdetermined.

3 Experimental Results and Evaluations

position accuracies [meter]		attitude accuracies [degree]	
σ_{north}	0.055	σ_{Roll}	0.002
σ_{east}	0.035	σ_{Pitch}	0.002
$\sigma_{altitude}$	0.069	σ_{Yaw}	0.005

Table 3.3: Accuracies of Exterior Orientations

Interior Orientations		accuracies	unit
focal length c	0.051	σ_c	6.9e-7 [meter]
x coordinate of principal point pp_x	-42.259	σ_{pp_x}	0.167 [μm]
x coordinate of principal point pp_y	115.384	σ_{pp_y}	0.799 [μm]

Table 3.4: Interior Orientations and their accuracies

DSM For each pair of stereo images, a disparity map is generated using Semi-Global Matching (SGM) algorithm. With disparity's property of being inversely proportional to depth, the disparity maps can be used to derive the DSM. Since SGM is a kind of appearance-based matching, the SGM-generated DSM is noisy in lowly textured regions. Thus, the DSM will be used only for setting up the initial values of the work flow, and will not influence the final results of the 3D lane marking reconstruction.

The DSM has 20 cm grid spacing. Figure 3.2 shows a part of the DSM. Standard deviations of the height value in this part of the DSM is shown in Figure 3.3. The number of stereo image pairs used for each part on the DSM is shown in Figure 3.4.

Orthorectified Images The orthorectified images are processed using the DSM and the interior and exterior orientations derived from the bundle adjustment. They are georeferenced and the scale is uniform. One of the orthorectified images is shown in Figure 3.6. The orthorectified images are only used for setting up initial values and used as intermediary step for processing the road masks, but do not influence the results of 3D lane marking reconstruction.

Road Masks Road segments are masked out from original images based on Open-StreetMap (OSM) data: Firstly, the rasterized road segments from OSM data are written with 25 meter buffer width around road axes into orthorectified images. By back-projecting the mask from orthorectified image to original image using the 3D information from the DSM, it can then be used to mask out the road regions on the original images, as shown in Figure 3.7.

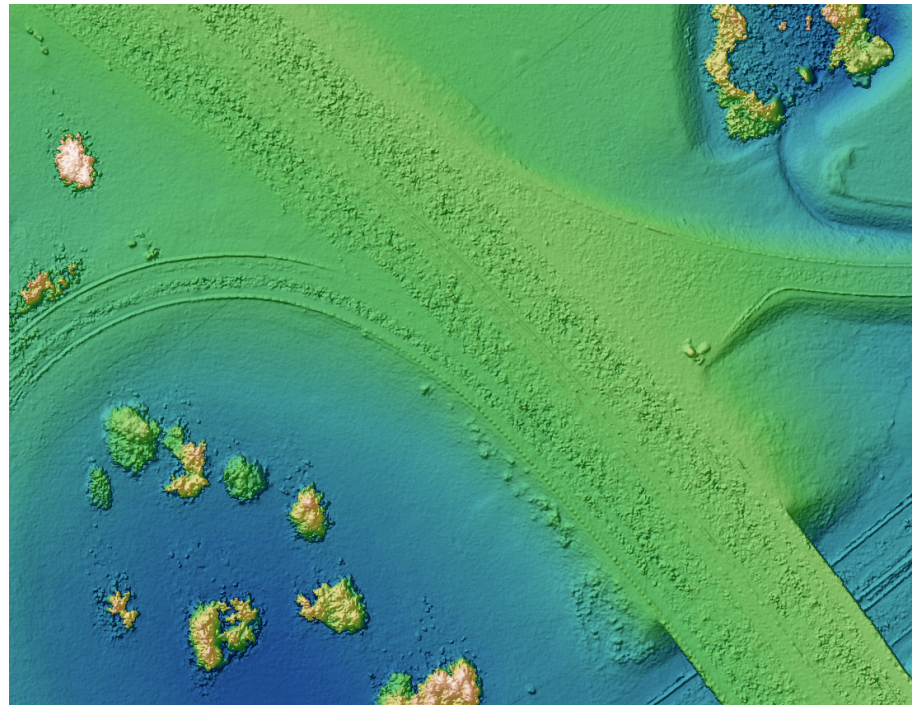


Figure 3.2: Part of the DSM in road area. It is noisy in the center of motorway.

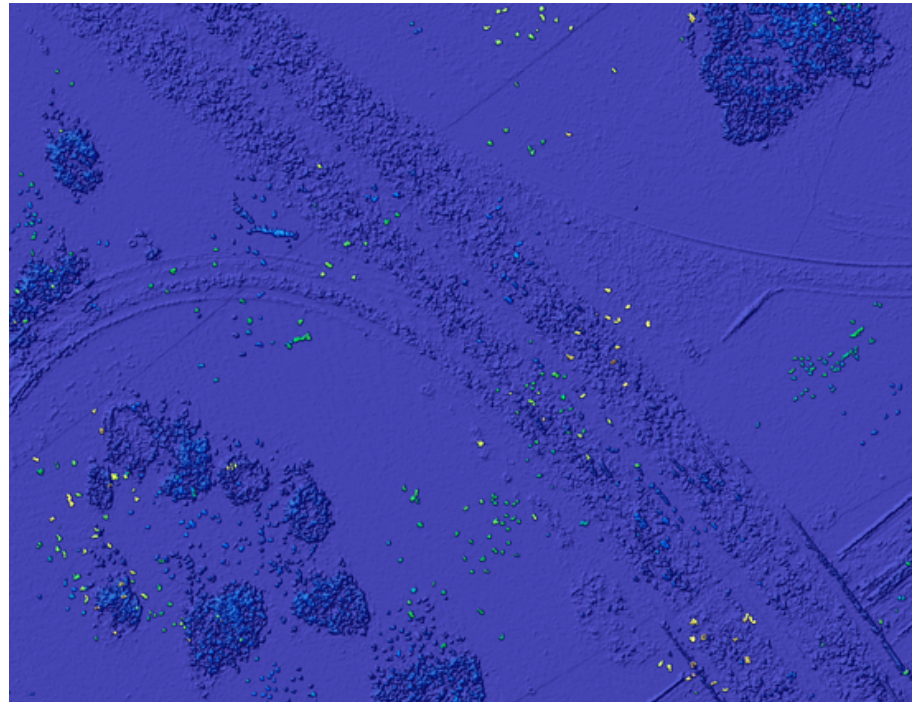


Figure 3.3: Standard deviations of the height value of the DSM in road area. It has higher value in the center of motorway.

3 Experimental Results and Evaluations

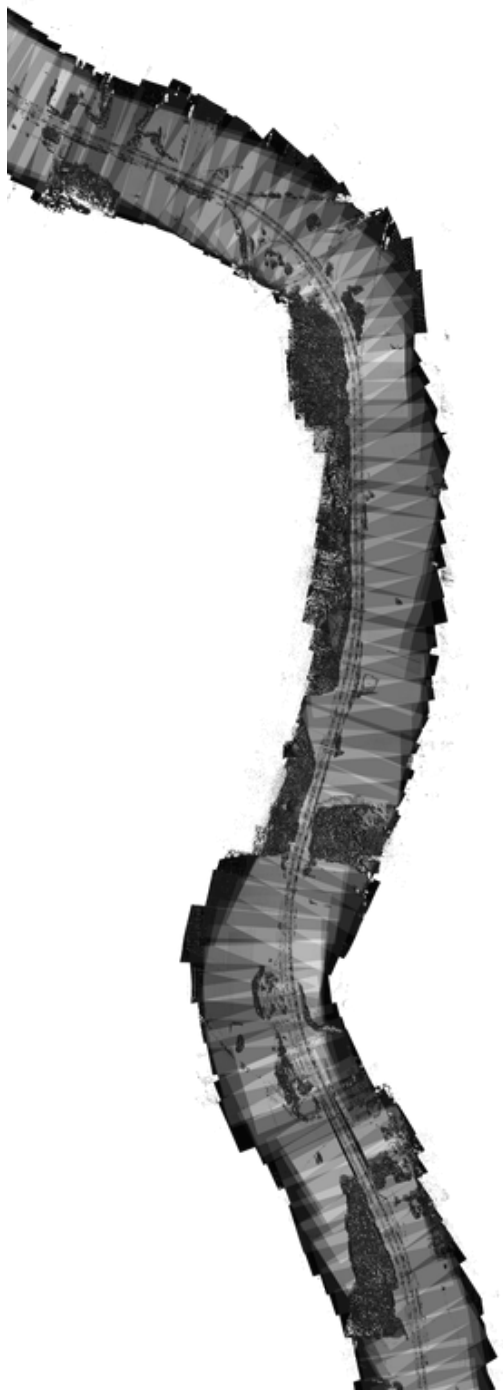


Figure 3.4: Distribution of stereo pairs used for DSM generation. Lighter color indicates more stereo pairs are used in that area. Maximum 27 stereo pairs are used for one pixel.



Figure 3.5: Original Image

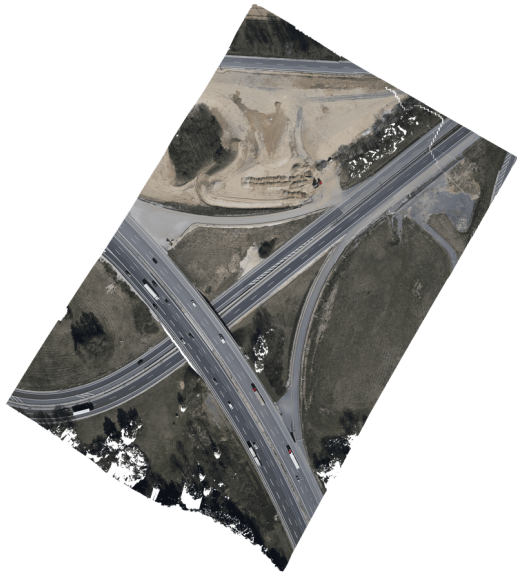


Figure 3.6: Orthorectified Image



Figure 3.7: Masked Image

3.2 Preprocessing

In lane marking extraction step, the σ value for Gaussian smoothing is set to be 1.8 to slightly suppress the noise in images. The extracted lines of length less than 70 pixels are rejected regarding the fact that a dashed lane-line is no longer than 6 meter which is correspondingly 87 pixels with GSD of 6.9 cm.

3.3 Simulation

This section aims to verify the correctness of the derived LS model and to discover some characteristics of the reconstruction model using simulation data. The used materials are as described in Section 3.1. Only the measurements (the image coordinates of the extracted lines), the true and approximate values of the unknowns (the object coordinates of a line segment) in the non-linear LS model are simulated, as described in Section 3.3.1.

Section 3.3.2 firstly evaluate if the iteration scheme converges to the correct solution given imperfect initial values of the unknowns. The significant height differences between the approximate and the reconstructed line segments are also presented, indicating the refining ability of the proposed reconstruction approach.

The ability of the derived LS model on detecting the measurement errors is then evaluated. Furthermore, how the increase of covering images would influence the reconstruction result is elaborated.

3.3.1 Simulation Data

The true line segment in object space Firstly, the object coordinates of the endpoints of a 3D line segment are defined, with 151.8 meters length, locating on the road surface in the test area (German highway A9) with 3 to 7 aerial images coverage. By linear interpolating several points with 0.2 meter spaces (considering DSM grid of 0.2 meter) between the two endpoints, a 3D line segment in the form of a set of 3D points is generated. This 3D line segment serves as the ground truth in the experiments in Section 3.3.

The observed line segments in image spaces The observations in the LS model are simulated by back-projecting the true line segment into the covering images. Gaussian random noise $e \sim \mathcal{N}(0, 0.5^2)$ is added in the observations for each LS adjustment, as line extraction process is of sub-pixel accuracy. The added noise is plotted in Figure 3.8

The approximate line segment in object space The initial estimates for non-linear LS adjustment is generated by projecting the observed line segments in image space onto the DSM.

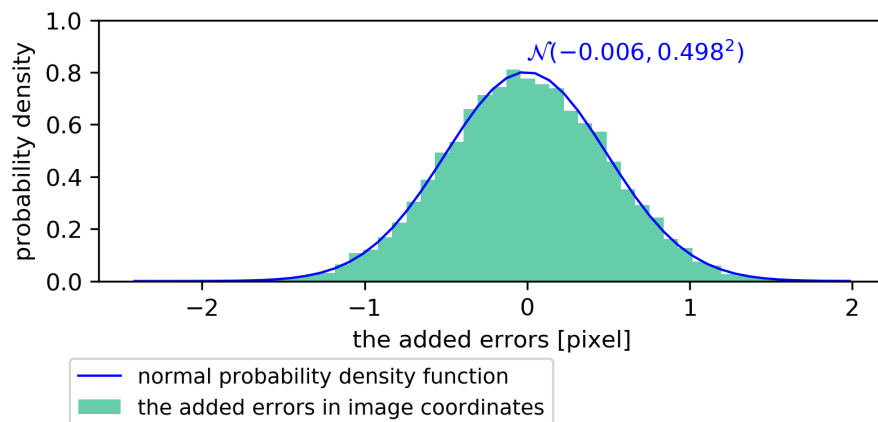


Figure 3.8: The added Gaussian random noise in the observations.

3 Experimental Results and Evaluations

3.3.2 Simulation Result

Figure 3.9 shows the reconstructed and the true line segments in UTM coordinate system (in Zone 32N). The distances from the reconstructed line nodes to the true line segment are computed and collected, resulting in sample size of 18. The sample mean is 0.008 [meter] and the sample variance is 0.101 [meter].

For such small sample size data, a two-tailed t-test is adopted to test if the population mean significantly not equals zero, i.e. **if the reconstructed line segments are significantly far from the true line segments**. Null hypothesis (H_0) and (two-tailed) alternative hypothesis (H_A) are stated as:

$$H_0 : \mu = 0$$
$$H_A : \mu \neq 0$$

A significance level $\alpha = 0.05$ is selected, with degree of freedom being $18 - 1 = 17$, the two-tailed t-table value $T_{(0.975,17)}$ is

$$T_{(0.975,17)} = 2.110$$

which leads to the decision rule: if test statistic T_{obs} is less than $-T_{(0.975,17)} = -2.110$ or greater than $T_{(0.975,17)} = 2.110$, reject the null hypothesis.

With the sample mean $\bar{x} = 0.008$, the proposed population mean $\mu_0 = 0$, the sample standard deviation $\sigma = 0.101$, and sample size $n = 18$, the test statistic for One Sample T Test has the calculated value:

$$T_{obs} = \frac{\bar{x} - \mu_0}{\sigma/\sqrt{n}} = \frac{0.008 - 0}{0.101/\sqrt{18}} \approx 0.34$$

which is neither less than $-T_{(0.975,17)} = -2.110$ nor greater than $T_{(0.975,17)} = 2.110$, i.e. not in the rejection region. As a result, we fail to reject the null hypothesis. In other words, **we are not able to claim that the reconstructed line is significantly far away from the true line**. This indicates that the derived non-linear LS adjustment model for 3D reconstruction is correct.

Figure 3.10 shows the reconstructed line segments and the DSM profile which serves as the initial approximation for non-linear LS adjustment, in UTM coordinate system (in Zone 32N). The maximum distance between them is 1.97 meter, mainly in Z-direction. This tells that **the reconstruction model is at least able to refine the initial approximation with 2 meters bias in Z-direction**.

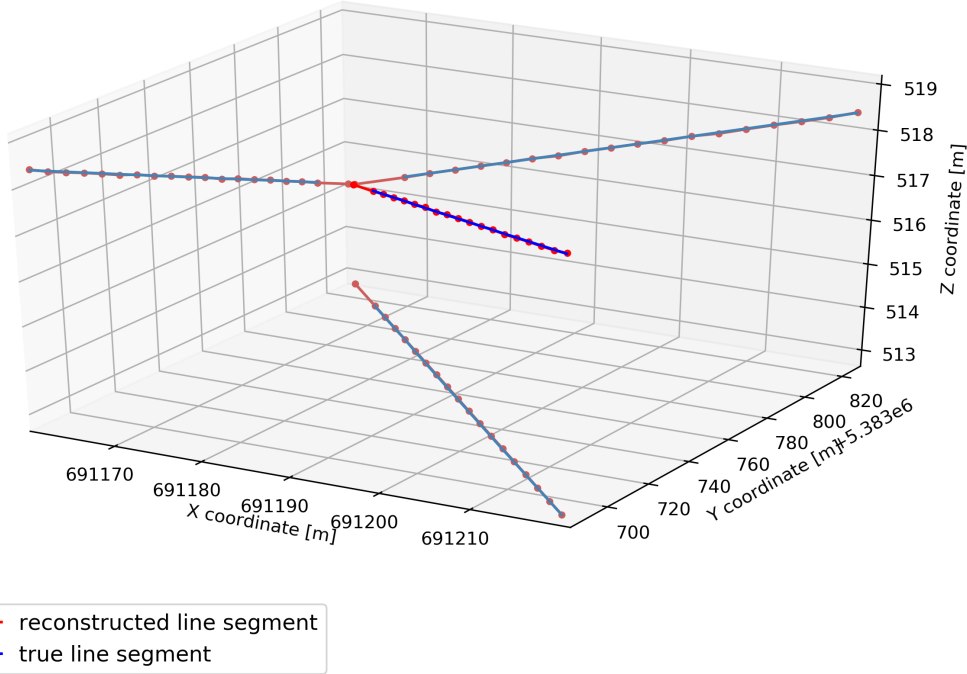


Figure 3.9: The reconstructed line segments and the true line segments in UTM coordinate system (in Zone 32N).

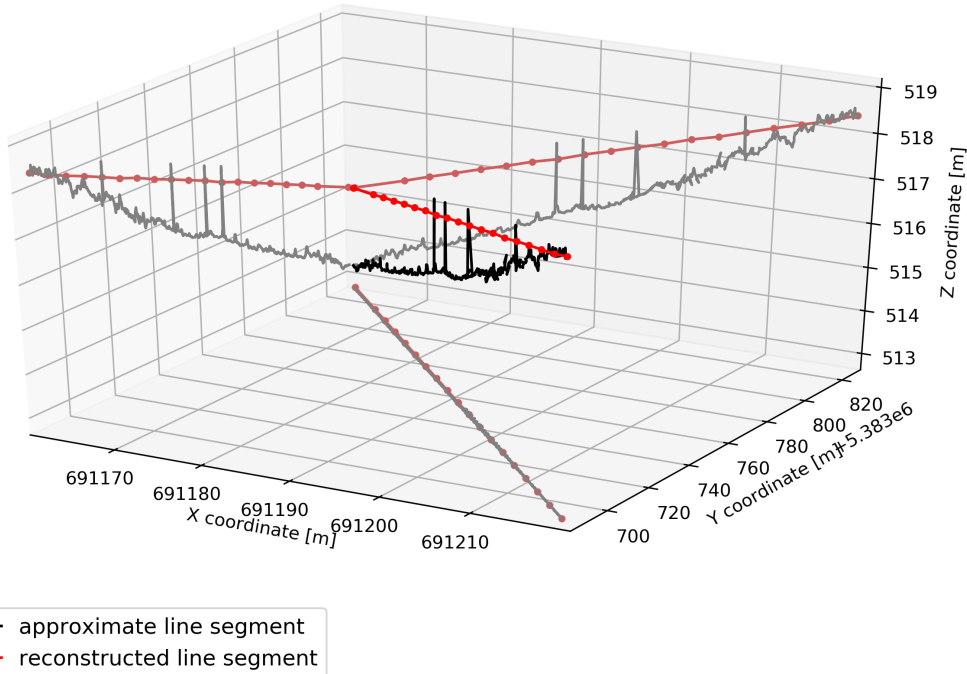


Figure 3.10: The reconstructed line segments and the unrefined DSM profile in UTM coordinate system (in Zone 32N).

3 Experimental Results and Evaluations

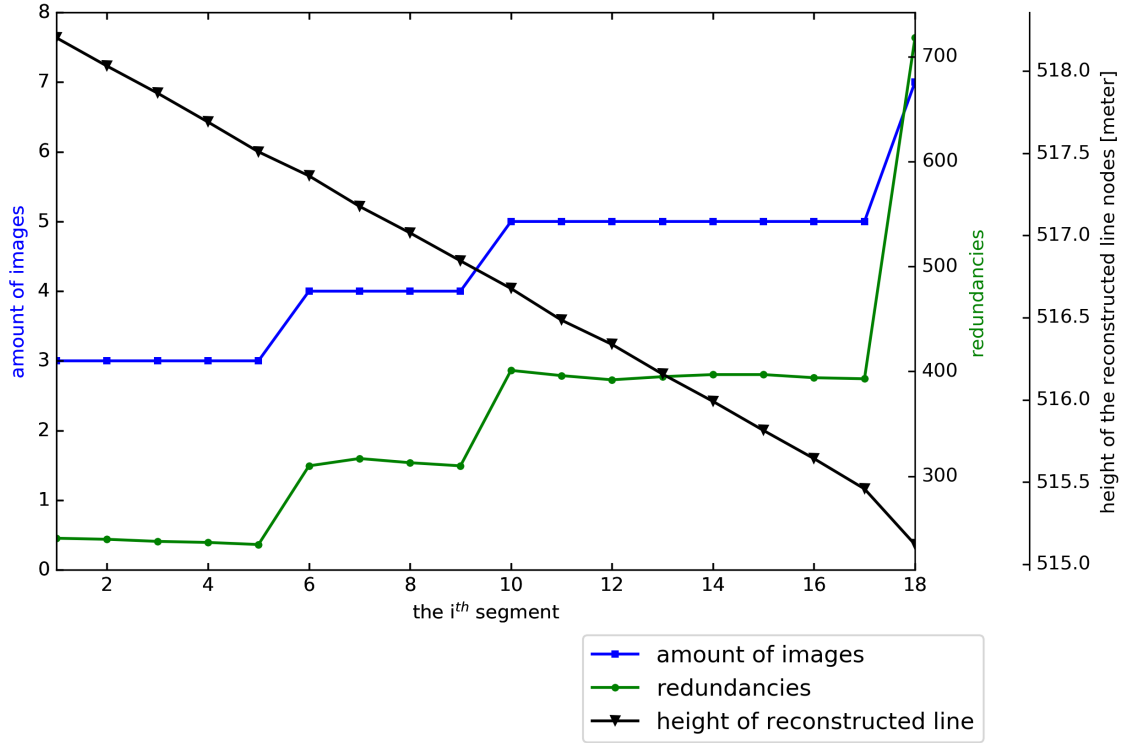


Figure 3.11: XXX.

Figure 3.11 gives the information on the amount of covering images, the redundancies and the height value of the reconstructed nodes, of each segment. Note that in each segment, LS adjustment is processed independently.

Figure 3.12 shows the mean and variance of the added random Gaussian noise and the adjusted residuals of each segment. This two samples are compared by applying a two-tailed two-sample T-test. Null hypothesis and alternative hypothesis (H_A) are stated as:

$$H_0 : \mu_1 - \mu_2 = 0$$

$$H_A : \mu_1 - \mu_2 \neq 0$$

With significance level $\alpha = 0.05$ and degree of freedom ≈ 300 , the t-score is

$$T_{0.975,300} = 1.968$$

As shown in Figure 3.13, all the test statistics T_{obs} of each segment are not less than $-T_{0.975,300} = -1.968$ or greater than $T_{0.975,300} = 1.968$, i.e. not in the rejection region, the null hypothesis could not be rejected. In other words, we fail to claim that the adjusted residuals are statistically different from the added random noise.

without the influence of imperfect camera parameters,

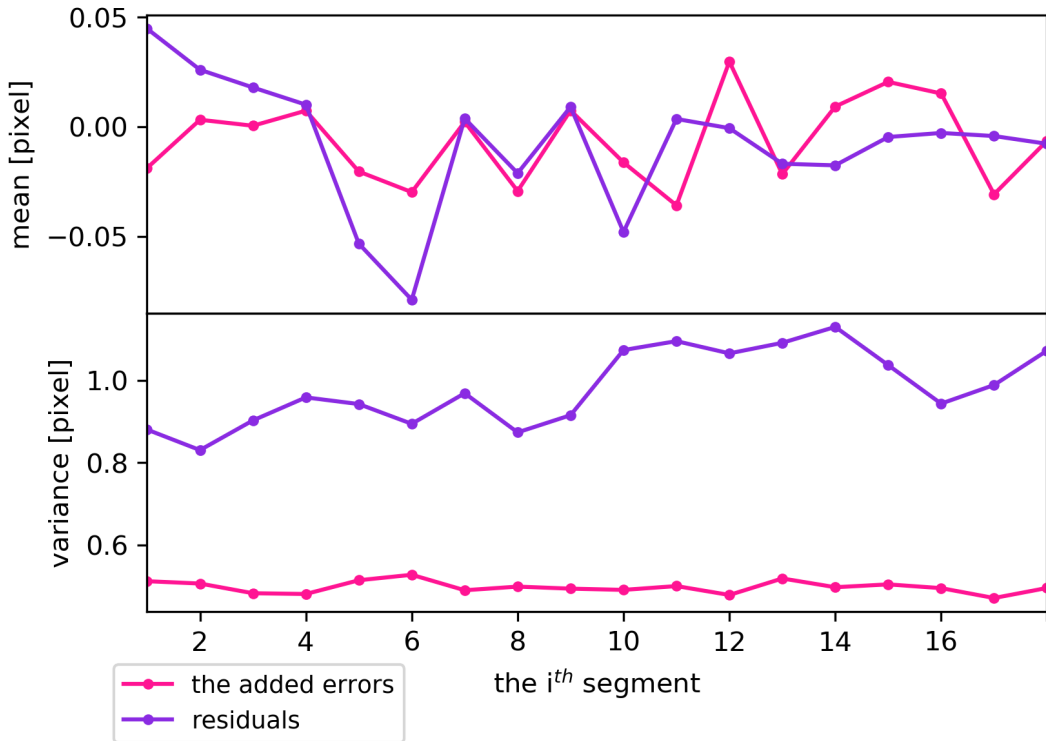


Figure 3.12: The relation between the added random Gaussian noise and the adjusted residuals.

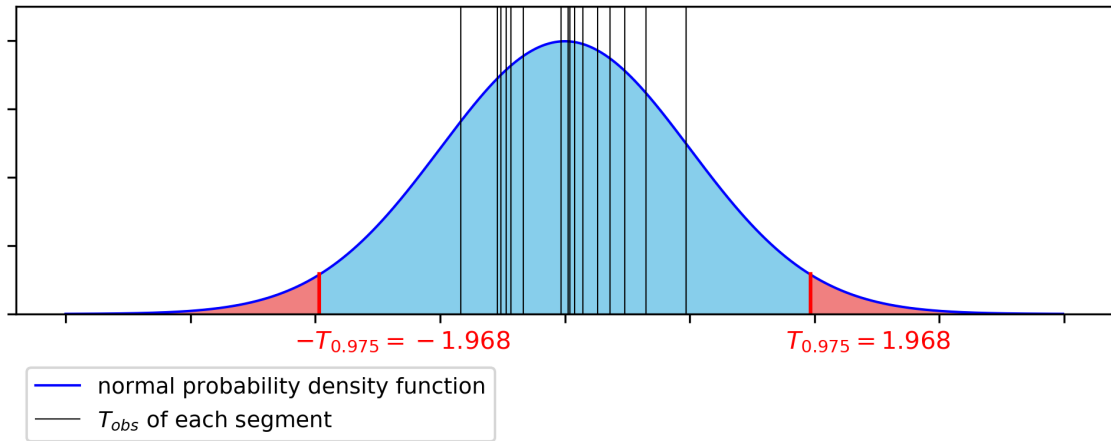


Figure 3.13: The red area under the probability density function is the rejection region, which is 5%. Since none of the T_{obs} falls in the rejection region, the null hypothesis could not be rejected.

3 Experimental Results and Evaluations

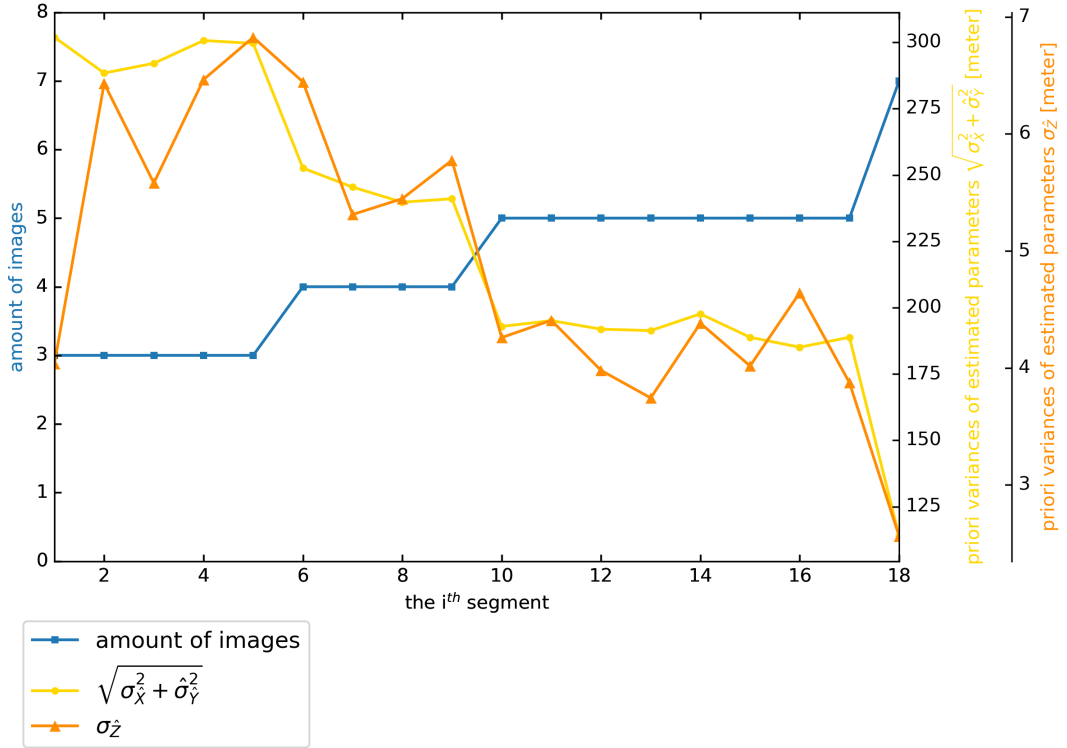


Figure 3.14: The relation between the variances of the estimated parameters and the amount of images.

From Figure 3.14 it can be seen that the estimated parameters generally have smaller prior variance values (in horizontal direction) $\sqrt{\sigma_X^2 + \hat{\sigma}_Y^2}$ and (in vertical direction) σ_Z with the increase of covering images. Whereas larger deviations from the trend are contained in vertical direction. **By increasing the configuration strength, i.e. increasing the amount of covering images with different orientations, the precision of the estimated parameters can be improved.**

Besides, the prior variance of the estimated parameters is smaller in vertical direction σ_Z than in horizontal direction $\sqrt{\sigma_X^2 + \hat{\sigma}_Y^2}$. This tells that **the reconstructed nodes have higher precision in vertical direction.** [reason? sec 3.1]

3.4 True Data

3.4.1 True Data Result

A continuous lane marking of 255.9 meters length is reconstructed. Figure 3.15 shows the reconstructed line segments and the DSM profile in UTM coordinate system (in Zone 32N). The distances from the reconstructed line segment to the DSM profile are computed and plotted into histogram in Figure 3.16. They are collected along the reconstructed line segments with 0.2 meter spacing (considering the DSM grid of 0.2 meter), resulting in sample size of 1256. The sample mean is -0.180 [meter] and the sample standard deviation is 0.174 [meter].

Assuming DSM height profile being significantly lower than the reconstructed line segments for more than 17??? centimeters, a lower-tailed Z-test is adopted. Null hypothesis (H_0) and (one-tailed) alternative hypothesis (H_A) are stated as:

$$\begin{aligned} H_0 : \mu &\geq -0.170 \\ H_A : \mu &< -0.170 \end{aligned}$$

A significance level $\alpha = 0.05$ is selected, i.e. the area in body is 0.950 out of 100%. The corresponding z-score is:

$$Z_{0.950} = 1.64$$

leads to the decision rule: if Z_{obs} is less than -1.64 , reject the null hypothesis.

With the sample mean $\bar{x} = -0.181$, the proposed population mean $\mu_0 = -0.170$, the sample standard deviation $\sigma = 0.174$, and sample size $n = 1256$, the test statistic for a One Sample Z Test has a calculated value:

$$Z_{obs} = \frac{\bar{x} - \mu_0}{\sigma/\sqrt{n}} = \frac{-0.181 - (-0.170)}{0.174/\sqrt{1256}} \approx -2.24$$

As the test statistic $Z_{obs} \approx -2.24$ is less than $-Z_{0.95} = -1.64$, i.e. in the rejection region, the null hypothesis is rejected. In other words, **with 95% confidence we can claim that the DSM profile is in average, statistically and significantly lower than the reconstructed line segments for at least 17 centimeters in this region.**

3 Experimental Results and Evaluations

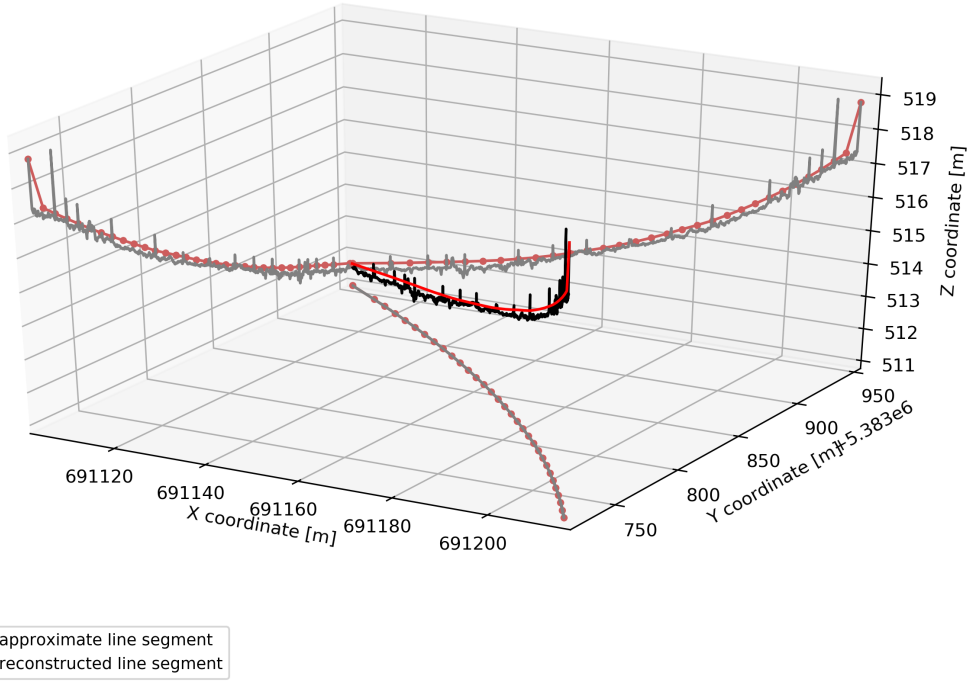


Figure 3.15: The reconstructed line segments and the unrefined DSM profile in UTM coordinate system (in Zone 32N).

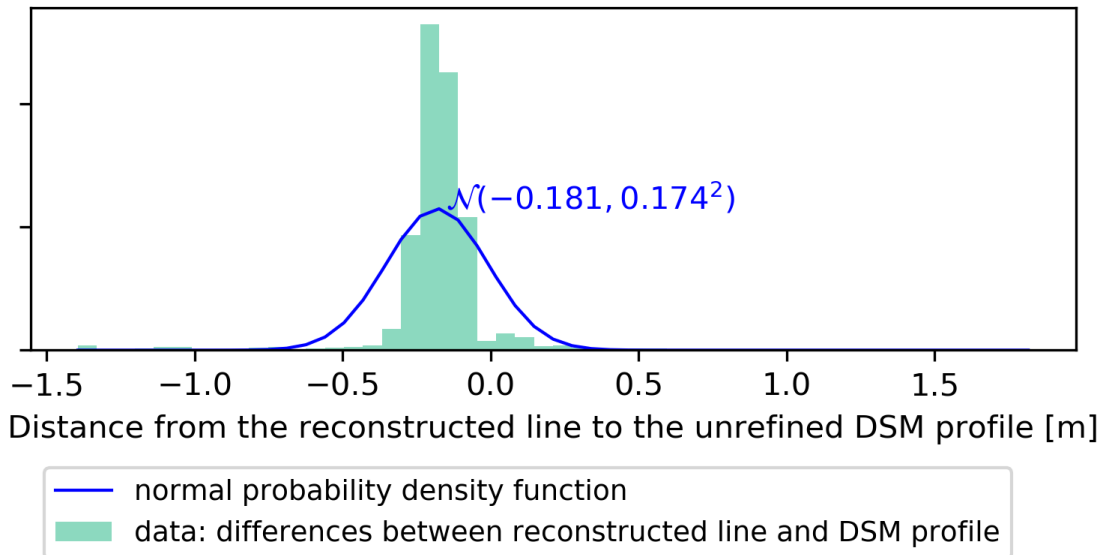


Figure 3.16: Histogram of the distances from the reconstructed line to the unrefined DSM profile.

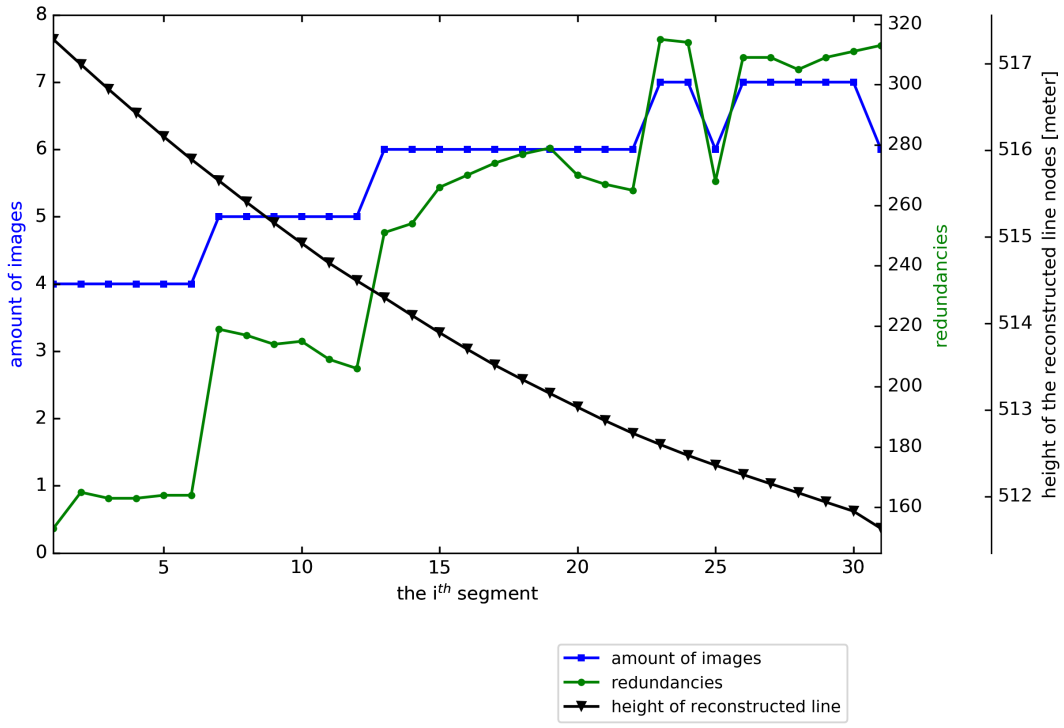


Figure 3.17: XXX...The relationship between image amount, the resulting reconstructed line segments, and the redundancies and posterior standard deviation in LS adjustment.

Figure 3.17 gives the information on the amount of covering images, the redundancies and the height value of the reconstructed nodes, of each segment. Note that in each segment, LS adjustment is processed independently.

Images configuration plays an important roll in 3D reconstruction.

Figure 3.19 shows:

3 Experimental Results and Evaluations

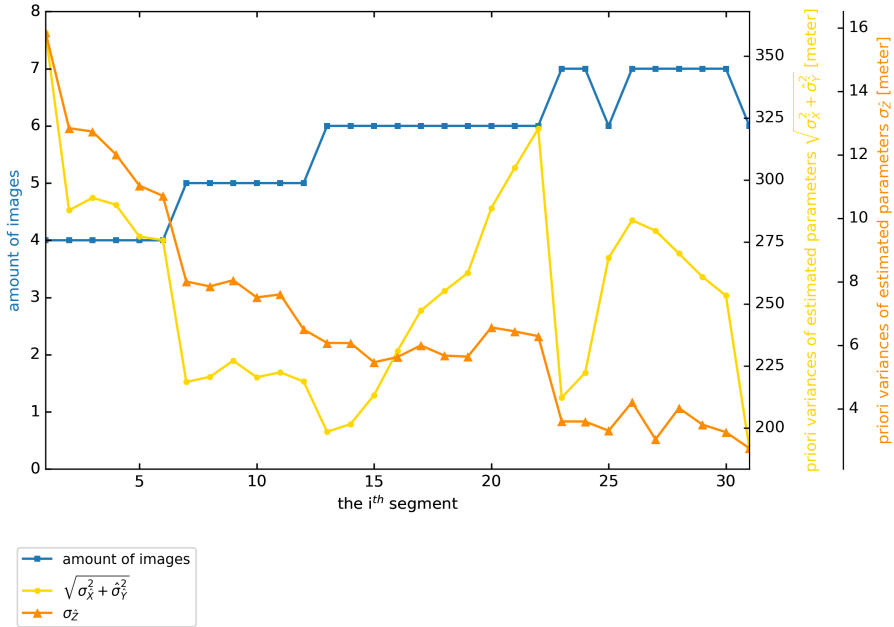


Figure 3.18: The variances of the estimated object coordinates, in horizontal and vertical directions.

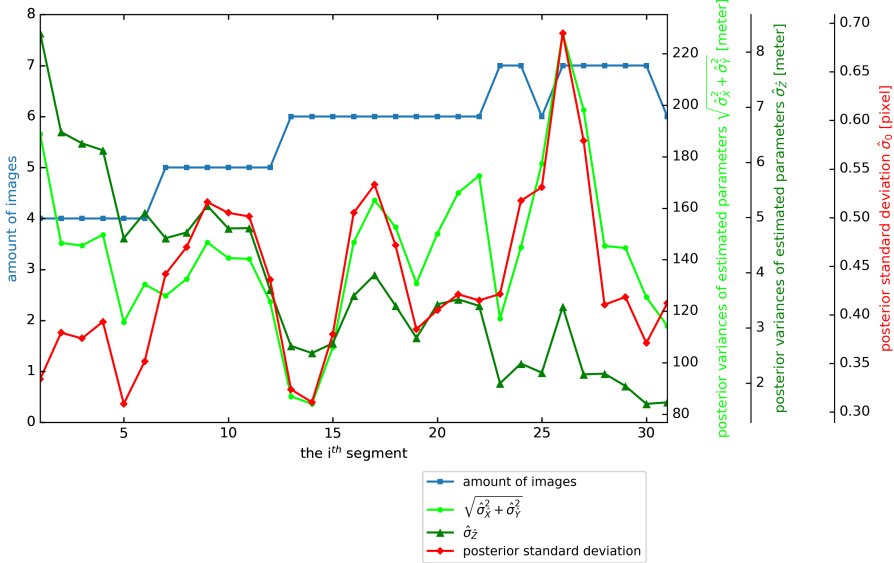


Figure 3.19: The estimated variances of the estimated object coordinates, in horizontal and vertical directions.

4 Conclusion and Future Work

Hier bitte einen kurzen Durchgang durch die Arbeit.

Ausblick

...und anschließend einen Ausblick

advantage our model can be used on lane markings reconstruction it not relying on textures or appearance-base matching

drawback unknown point-to-point relationship in image space, endpoints correspondence rely on quality of orientations

A LaTeX-Tipps

Probleme kann man niemals mit
derselben Denkweise lösen,
durch die sie entstanden sind.

(Albert Einstein)

Pro Satz eine neue Zeile. Das ist wichtig, um sauber versionieren zu können. In LaTeX werden Absätze durch eine Leerzeile getrennt.

Folglich werden neue Abstätze insbesondere *nicht* durch Doppelbackslashes erzeugt. Der letzte Satz kam in einem neuen Absatz.

A.1 File-Encoding und Unterstützung von Umlauten

Die Vorlage wurde 2010 auf UTF-8 umgestellt. Alle neueren Editoren sollten damit keine Schwierigkeiten haben.

A.2 Zitate

Referenzen werden mittels `\cite[key]` gesetzt. Beispiel: **[WSPA]** oder mit Autorenangabe: **WSPA**.

Der folgende Satz demonstriert 1. die Großschreibung von Autorennamen am Satzanfang, 2. die richtige Zitation unter Verwendung von Autorennamen und der Referenz, 3. dass die Autorennamen ein Hyperlink auf das Literaturverzeichnis sind sowie 4. dass in dem Literaturverzeichnis der Namenspräfix “van der” von “Wil M. P. van der Aalst” steht. **RVvdA2016** präsentieren eine Studie über die Effektivität von Workflow-Management-Systemen.

Der folgende Satz demonstriert, dass man mittels `\label` in einem Bibliographie“=Eintrag den Textteil des generierten Labels überschreiben kann, aber das Jahr und die Eindeutigkeit noch von biber generiert wird. Die Apache ODE Engine **[ApacheODE]** ist eine Workflow-Maschine, die BPEL-Prozesse zuverlässig ausführt.

Wörter am besten mittels `\enquote{...}` “einschließen”, dann werden die richtigen Anführungszeichen verwendet.

Beim Erstellen der Bibtex-Datei wird empfohlen darauf zu achten, dass die DOI aufgeführt wird.

Listing A.1 lstlisting in einer Listings-Umgebung, damit das Listing durch Balken abgetrennt ist

```
<listing name="second sample">
<content>not interesting</content>
</listing>
```

A.3 Mathematische Formeln

Mathematische Formeln kann man *so* setzen. `symbols-a4.pdf` (zu finden auf <http://www.ctan.org/tex-archive/info/symbols/comprehensive/symbols-a4.pdf>) enthält eine Liste der unter LaTeX direkt verfügbaren Symbole. Z. B. \mathbb{N} für die Menge der natürlichen Zahlen. Für eine vollständige Dokumentation für mathematischen Formelsatz sollte die Dokumentation zu `amsmath`, <ftp://ftp.ams.org/pub/tex/doc/amsmath/> gelesen werden.

Folgende Gleichung erhält keine Nummer, da `\equation*` verwendet wurde.

$$x = y$$

Die Gleichung A.1 erhält eine Nummer:

$$x = y \tag{A.1}$$

Eine ausführliche Anleitung zum Mathematikmodus von LaTeX findet sich in <http://www.ctan.org/tex-archive/help/Catalogue/entries/voss-mathmode.html>.

A.4 Quellcode

Listing A.1 zeigt, wie man Programmlistings einbindet. Mittels `\lstinputlisting` kann man den Inhalt direkt aus Dateien lesen.

Quellcode im `<listing />` ist auch möglich.

A.5 Abbildungen

Die Figure A.1 und A.2 sind für das Verständnis dieses Dokuments wichtig. Im Anhang zeigt Figure A.4 on page 52 erneut die komplette Choreographie.

Es ist möglich, SVGs direkt beim Kompilieren in PDF umzuwandeln. Dies ist im Quellcode zu `latex-tipps.tex` beschrieben, allerdings auskommentiert.

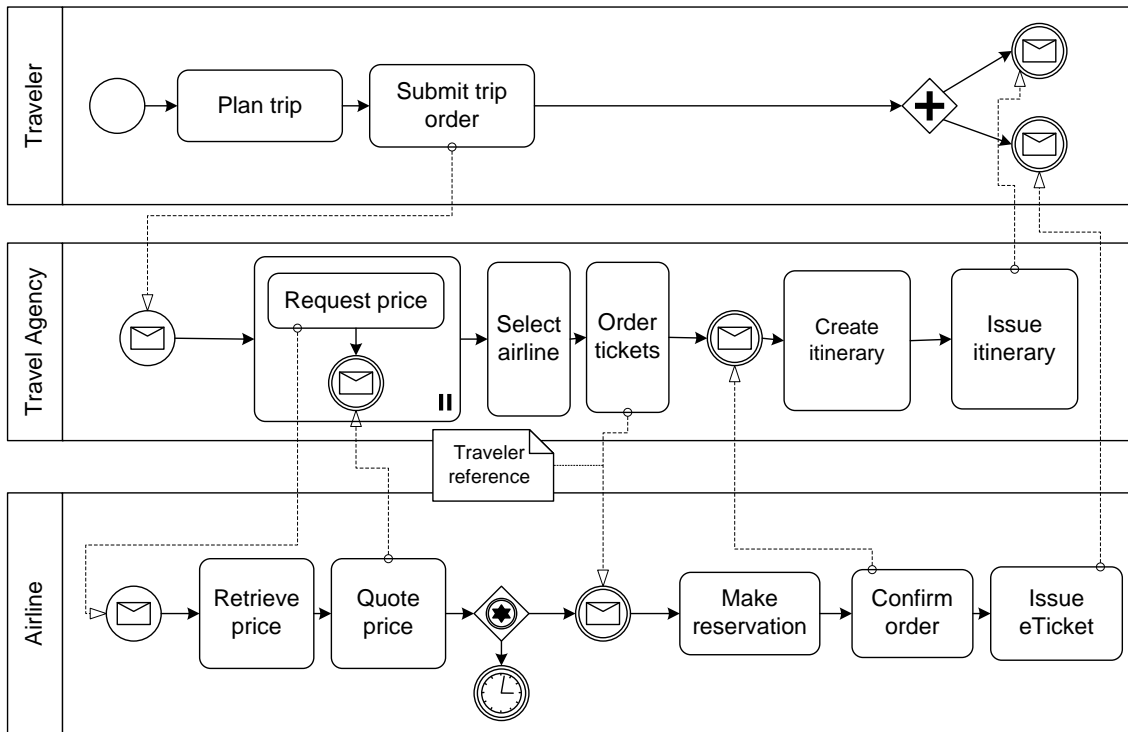


Figure A.1: Beispiel-Choreographie

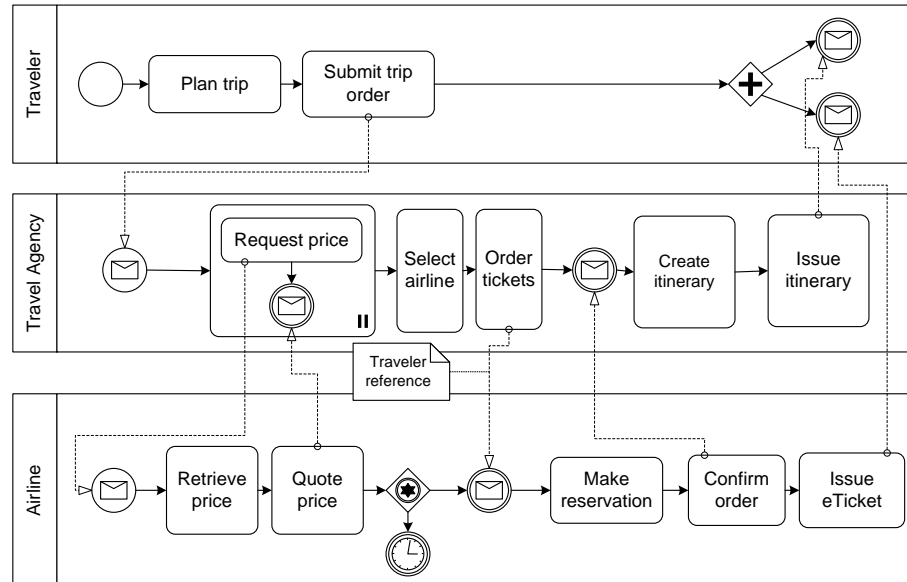


Figure A.2: Die Beispiel-Choreographie. Nun etwas kleiner, damit \textwidth demonstriert wird. Und auch die Verwendung von alternativen Bildunterschriften für das Verzeichnis der Abbildungen. Letzteres ist allerdings nur Bedingt zu empfehlen, denn wer liest schon so viel Text unter einem Bild? Oder ist es einfach nur Stilsache?

A LaTeX-Tipps

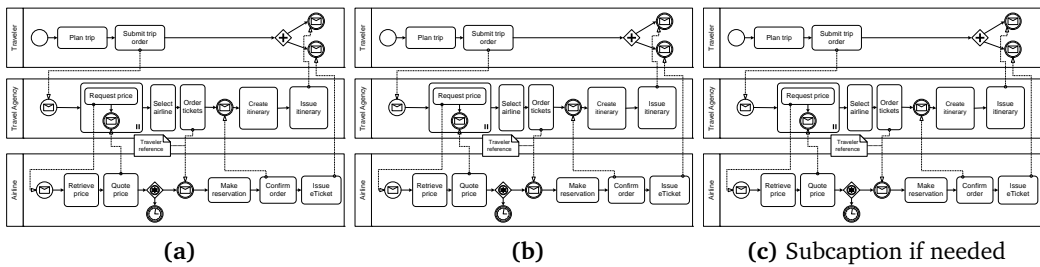


Figure A.3: Beispiel um 3 Abbildung nebeneinader zu stellen nur jedes einzeln referenziern zu können. Abbildung A.3b ist die mittlere Abbildung.

zusammengefasst	Titel
Tabelle wie in tabsatz.pdf empfohlen gesetzt	
Beispiel ein schönes Beispiel für die Verwendung von “multirow”	

Table A.1: Beispieltabelle – siehe <http://www.ctan.org/tex-archive/info/german/tabsatz/>

A.6 Tabellen

Table A.1 zeigt Ergebnisse und die Table A.1 zeigt wie numerische Daten in einer Tabelle representiert werden können.

A.7 Pseudocode

Algorithm A.1 zeigt einen Beispielalgorithmus.

Bedingungen	Parameter 1		Parameter 2		Parameter 3		Parameter 4	
	M	SD	M	SD	M	SD	M	SD
W	1.1	5.55	6.66	.01				
X	22.22	0.0	77.5	.1				
Y	333.3	.1	11.11	.05				
Z	4444.44	77.77	14.06	.3				

Table A.2: Beispieltabelle für 4 Bedingungen (W-Z) mit jeweils 4 Parameters mit (M und SD). Hinweis: immer die selbe anzahl an Nachkommastellen angeben.

Algorithm A.1 Sample algorithm

```

procedure SAMPLE( $a, v_e$ )
    parentHandled  $\leftarrow (a = \text{process}) \vee \text{visited}(a'), (a', c, a) \in \text{HR}$ 
                //  $(a', c, a) \in \text{HR}$  denotes that  $a'$  is the parent of  $a$ 
    if parentHandled  $\wedge (\mathcal{L}_{in}(a) = \emptyset \vee \forall l \in \mathcal{L}_{in}(a) : \text{visited}(l)) then
        visited( $a$ )  $\leftarrow \text{true}$ 
        writeso( $a, v_e$ )  $\leftarrow \begin{cases} \text{joinLinks}(a, v_e) & |\mathcal{L}_{in}(a)| > 0 \\ \text{writes}_o(p, v_e) & \exists p : (p, c, a) \in \text{HR} \\ (\emptyset, \emptyset, \emptyset, \text{false}) & \text{otherwise} \end{cases}$ 
        if  $a \in \mathcal{A}_{\text{basic}}$  then
            HANDLEBASICACTIVITY( $a, v_e$ )
        else if  $a \in \mathcal{A}_{\text{flow}}$  then
            HANDLEFLOW( $a, v_e$ )
        else if  $a = \text{process}$  then // Directly handle the contained activity
            HANDLEACTIVITY( $a', v_e$ ),  $(a, \perp, a') \in \text{HR}$ 
            writes•( $a$ )  $\leftarrow \text{writes}_•(a')$ 
        end if
        for all  $l \in \mathcal{L}_{out}(a)$  do
            HANDLELINK( $l, v_e$ )
        end for
    end if
end procedure$ 
```

A LaTeX-Tipps

Und wer einen Algorithmus schreiben möchte, der über mehrere Seiten geht, der kann das nur mit folgendem **üblen** Hack tun:

Algorithmus A.2 Description

code goes here

test2

A.8 Abkürzungen

Beim ersten Durchlauf betrug die Fehlerrate (FR) 5. Beim zweiten Durchlauf war die FR 3. Die Pluralform sieht man hier: error rates (ERs). Um zu demonstrieren, wie das Abkürzungsverzeichnis bei längeren Beschreibungstexten aussieht, muss hier noch Relational Database Management Systems (RDBMS) erwähnt werden.

Mit `\gls{...}` können Abkürzungen eingebaut werden, beim ersten Aufrufen wird die lange Form eingesetzt. Beim wiederholten Verwenden von `\gls{...}` wird automatisch die kurz Form angezeigt. Außerdem wird die Abkürzung automatisch in die Abkürzungsliste eingefügt. Mit `\glspl{...}` wird die Pluralform verwendet. Möchte man, dass bei der ersten Verwendung direkt die Kurzform erscheint, so kann man mit `\glsunset{...}` eine Abkürzung als bereits verwendet markieren. Das Gegenteil erreicht man mit `\glsreset{...}`.

Definiert werden Abkürzungen in der Datei *content ausarbeitung.tex* mithilfe von `\newacronym{...}{...}{...}`.

Mehr Infos unter: <http://tug.ctan.org/macros/latex/contrib/glossaries/glossariesbegin.pdf>

A.9 Verweise

Für weit entfernte Abschnitte ist “varioreref” zu empfehlen: “Siehe Appendix A.3 on page 46”. Das Kommando `\vref` funktioniert ähnlich wie `\cref` mit dem Unterschied, dass zusätzlich ein Verweis auf die Seite hinzugefügt wird. `vref:` “Appendix A.1 on page 45”, `cref:` “Appendix A.1”, `ref:` “A.1”.

Falls “varioreref” Schwierigkeiten macht, dann kann man stattdessen “cref” verwenden. Dies erzeugt auch das Wort “Abschnitt” automatisch: Appendix A.3. Das geht auch für Abbildungen usw. Im Englischen bitte `\Cref{...}` (mit großem “C” am Anfang) verwenden.

A.10 Definitionen

Definition A.10.1 (Title)

Definition Text

Definition A.10.1 zeigt ...

A.11 Fußnoten

Fußnoten können mit dem Befehl `\footnote{...}` gesetzt werden¹. Mehrfache Verwendung von Fußnoten ist möglich indem man zuerst ein Label in der Fußnote setzt `\footnote{\label{...}}...` und anschließend mittels `\cref{...}` die Fußnote erneut verwendet¹.

A.12 Verschiedenes

KAPITÄLCHEN werden schön gesperrt...

- I. Man kann auch die Nummerierung dank paralist kompakt halten
- II. und auf eine andere Nummerierung umstellen

A.13 Weitere Illustrationen

Figures A.4 and A.5 zeigen zwei Choreographien, die den Sachverhalt weiter erläutern sollen. Die zweite Abbildung ist um 90 Grad gedreht, um das Paket `pdflscape` zu demonstrieren.

¹Diese Fußnote ist ein Beispiel.

A LaTeX-Tipps

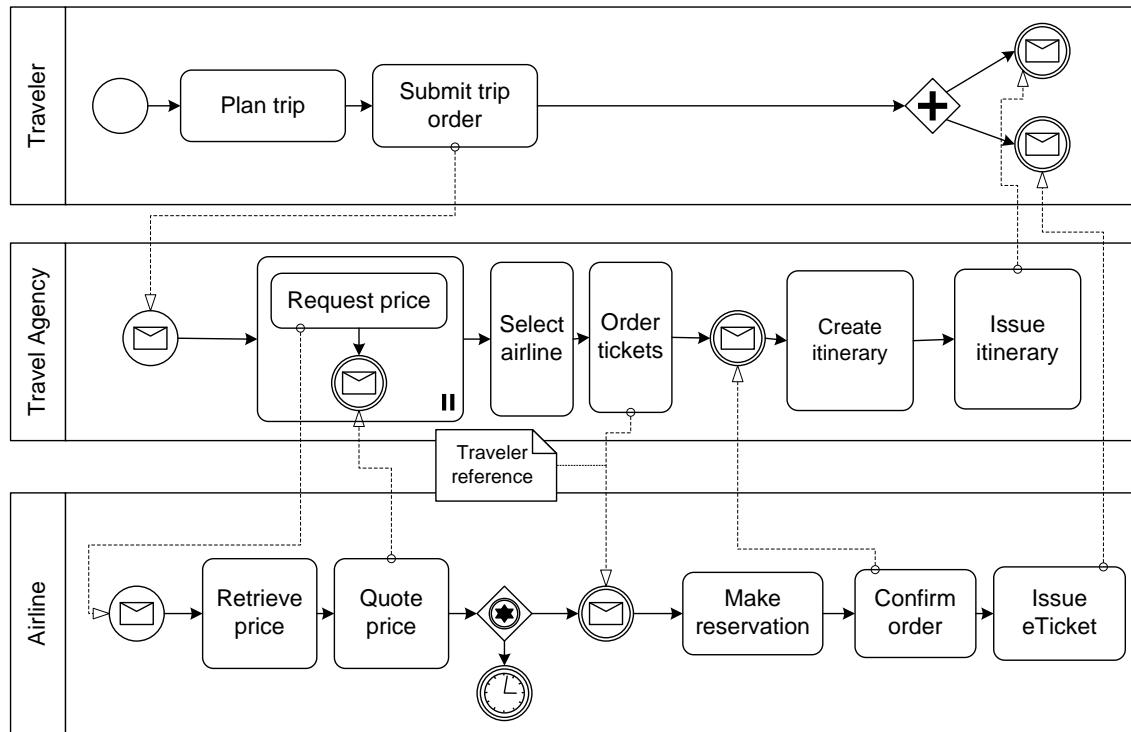


Figure A.4: Beispiel-Choreographie I

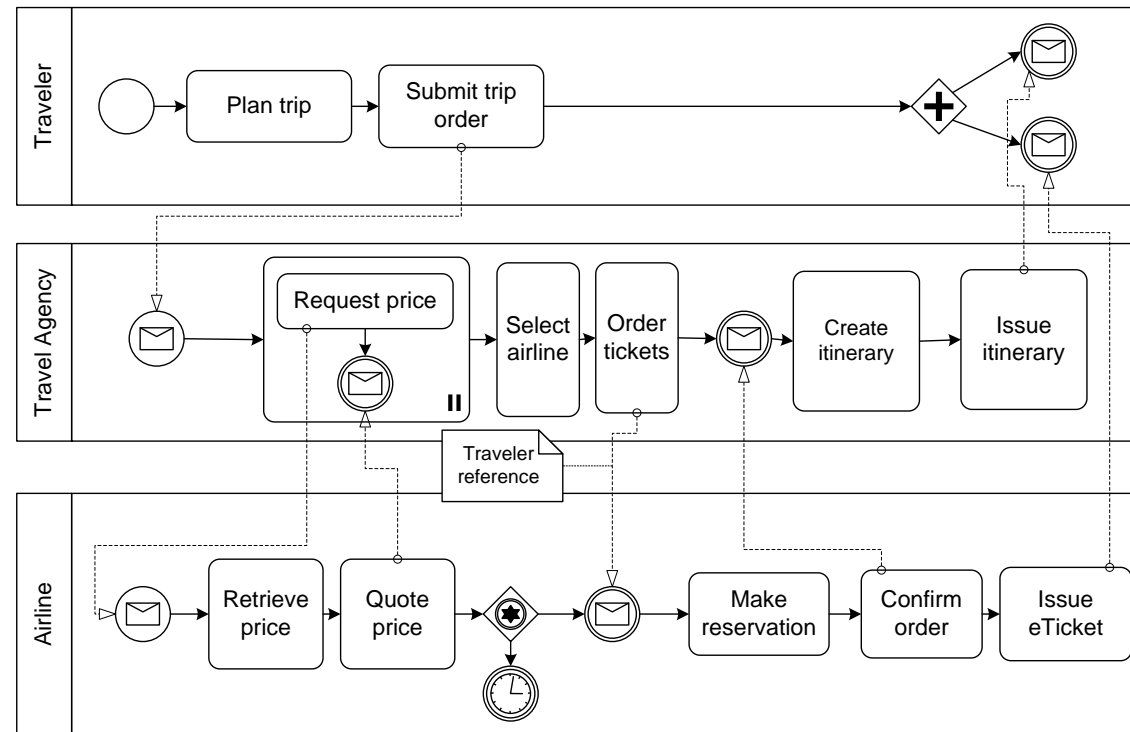


Figure A.5: Beispiel-Choreographie II

A.14 Plots with pgfplots

Pgfplot ist ein Paket um Graphen zu plotten ohne den Umweg über gnuplot oder matplotlib zu gehen.

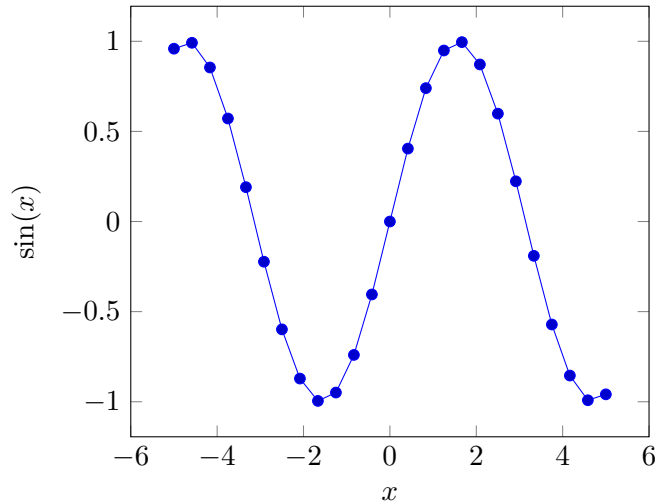


Figure A.6: $\sin(x)$ mit pgfplots.

A.15 Figures with tikz

TikZ ist ein Paket um Zeichnungen mittels Programmierung zu erstellen. Dieses Paket eignet sich um Gitter zu erstellen oder andere regelmäßige Strukturen zu erstellen.

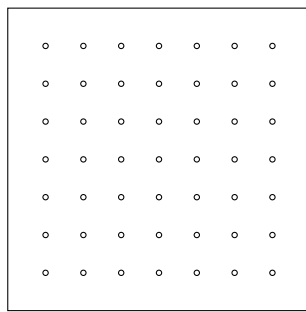


Figure A.7: Eine tikz-Graphik.

A.16 Schlusswort

Verbesserungsvorschläge für diese Vorlage sind immer willkommen. Bitte bei GitHub ein Ticket eintragen (<https://github.com/latextemplates/uni-stuttgart-computer-science-template/issues>).

All links were last followed on December 22, 2017.

Declaration

I hereby declare that the work presented in this thesis is entirely my own and that I did not use any other sources and references than the listed ones. I have marked all direct or indirect statements from other sources contained therein as quotations. Neither this work nor significant parts of it were part of another examination procedure. I have not published this work in whole or in part before. The electronic copy is consistent with all submitted copies.

place, date, signature